PHYSICAL REVIEW C VOLUME 23, NUMBER 1 JANUARY 1981

Density patterns and energy-angle distributions from a simple cascade scheme for fast $^{20}Ne + ^{238}U$ collisions

E. C. Halbert
Oak Ridge National Laboratory, Oak Ridge, Tennessee 37830
(Received 25 March 1980)

A simple but fully three-dimensional cascade approach, appropriate for considering heavy-ion collisions at a few hundred MeV per projectile nucleon, is applied to $^{20}Ne + ^{238}U$. For impact parameters b_{NeU} of 0 and 5 fm the calculated results include densities $\rho(\vec{r},t)$ of nucleon masses during the collision and energy-angle distributions $d^2n/dEd\Omega$ of scattered nucleon masses emerging from the collision. All of the present calculations use idealized nucleon-nucleon interactions implying cross sections σ_{NN} that are purely elastic, isotropic, and independent of the initial NN state. Some of these calculations also introduce excluded-volume effects, such as those associated with a classical hard core in the NN interaction. The calculated density $\rho(\vec{r},t)$ is quite sensitive to changes in the size of the excluded volume (we tried hard cores of radius 0, 0.5, and 0.9 fm). However, it is only in the case of zero excluded volume that $\rho(\vec{r},t)$ shows much sensitivity to changes in σ_{NN} (we tried $\sigma_{NN} = 15.4$, 25.4, and 53.1 mb). The distribution $d^2n/dEd\Omega$ is rather insensitive to the excluded-volume feature but does depend sensitively on σ_{NN}, on the impact parameter b_{NeU}, and on the emitted-nucleon characteristics E and Ω. For one particular set of NN parameters—hard-core radius = 0.9 fm, $\sigma_{NN} = 25.4$ mb—our cascade calculation reduces to a case in which each nucleon is modeled precisely as a classical frictionless billiard ball (a "hard sphere") of diameter equal to the hard-core radius. For this case our cascade results would be especially suitable for comparison with analogous fluid-dynamic results—these latter to be computed using the known equation of state of a hard-sphere gas.

[NUCLEAR REACTIONS High-energy heavy-ion reactions. Intranuclear cascade calculations. $^{20}Ne + ^{238}U$ collisions at laboratory energies of about 200–400 MeV per nucleon of the projectile. Density of nuclear matter. Energy-angle distributions of emitted nucleons.]

I. INTRODUCTION

High-energy heavy-ion collisions ($E^{LAB}_{BEAM} = 100$–2000 MeV per nucleon) are currently receiving much attention, both experimental and theoretical.[1-9] There is special interest in central collisions, where "central" implies that the nucleus-nucleus impact parameter is small enough so that a large fraction of the projectile matter makes geometric contact with target matter. For such collisions there is a chance of attaining nuclear-matter densities several times ground-state density, and an associated possibility of developing exotic phenomena (e.g., density isomers, pion condensates, quark matter). Several years ago there was widespread optimism that, without very strenuous efforts either experimental or theoretical, physicists would soon find, in experimental data, clear manifestations of exotic phenomena.[10] That optimism has since diminished. It now seems that most of the already collected experimental data can probably be explained in terms of ordinary nonexotic phenomena, and that models which assume the development of exotic phenomana during collision often predict final-state observables very similar to what can be predicted without assuming any exotic phenomena. These circumstances motivate intensified efforts of two kinds:

(a) to identify and focus on observables sensitive to transient exotic phenomena; but also

(b) to carefully investigate "ordinary" phenomena, i.e., to study the *consequences* of assuming that in high-energy collisions of many-nucleon systems, there are only mild changes in the nuclear properties and processes already familiar from few-nucleon systems and low-energy many-nucleon systems.

In this paper we report an investigation of type (b), involving only ordinary phenomena.

Even when one is restricting attention to ordinary phenomena, it makes sense to consider results from a variety of theoretical approaches, because at present there is no single method which is tractable and also *a priori* well justified. Some of the methods exploited recently are fireball,[11] firestreak,[12] rows on rows,[13] single-scattering knockout,[14] fluid dynamics,[15-20] cascade[15,21-29] (sometimes followed by statistical evaporation), and many-body classical equations of motion[25,30-32] using NN potentials.[33] By and large, these methods use classical concepts. One way in which these methods differ from each other is in the

rigidity of their assumptions about the achievement of global or local equilibrium within specified geometric zones.

The theoretical results reported in this paper were obtained by using a simple three-dimensional cascade scheme, SIMON.[27-29] It is a simulation code in which each nucleus-nucleus collision consists of explicit nucleon-nucleon scatterings. SIMON 's basic character[27,28] is intermediate between those of a conventional cascade method[21-24] incorporating *NN* cross sections, and a classical equations-of-motion method (CEOM)[25,30-32] incorporating *NN* forces.[33,34] In the present SIMON calculations we use idealized physical features. For example, we use *NN* interactions consistent with an *NN* cross section that is purely elastic, isotropic, and energy independent. However, in comparison with some other approaches (fireball, firestreak, rows on rows, or fluid dynamics), SIMON is relative free of presupposed geometric constraints and presupposed equilibrium conditions. That is why it seems worthwhile to examine some geometric and energetic aspects of heavy-ion collisions modeled with SIMON . In this paper we apply SIMON to collisons of ^{20}Ne with ^{238}U for Ne beam energies of several hundred MeV per nucleon. We report calculated densities $\rho(\vec{r}, t)$ of nucleon matter during collision, and also energy-angle distributions $d^2n/dEd\cos\theta$ of scattered matter emerging from collision. These quantities are computed for impact parameters b_{NeU} of 0 and 5 fm. The results that we display are *ensemble averages*, where an ensemble is a set of many ($\approx$300) ^{20}Ne + ^{238}U collisions all identical in their nucleus-nucleus impact parameter but randomly different in some details of the nucleon degrees of freedom.

Our results for $\rho(\vec{r}, t)$ and $d^2n/dE\,d\cos\theta$ might be closer to reality if, instead of being calculated from the simple SIMON code, they had been calculated with one of the present-day cascade codes incorporating more realistic (energy- and angle-dependent) *NN* cross sections. Such codes have been used to produce results that agree nicely with many experimentally determined "end-of-collision" data, e.g., inclusive emission cross sections and two-particle correlations in emission. (See especially Refs. 22 and 23.) However, SIMON has some features which are not in any of the conventional cascade[21-24,34] codes. In particular, SIMON has no need of depletion or rearrangement recipes,[59] and SIMON allows the adjustment of excluded-volume effects such as those associated with a classical hard core in the *NN* interaction. We have calculated results for several different sizes of the excluded volume, and also several different magnitudes of the assumed nucleon-nucleon cross section σ_{NN}.

The basic scheme of SIMON could be retained while refining the code to include more realistic details such as energy-dependent *NN* cross sections and Pauli-principle corrections.[29] However, improved realism is not the direction in which the present study extends work that was reported in the first few papers[27,28,15] about SIMON . Rather, our present study involves (a) some broadening in the range of idealized *NN* scattering models, and (b) a more thorough investigation of the consequent particle-density patterns and energy-angle distributions. Obviously, our main concern in this paper is not the close reproduction of measured data. Rather, our main concerns are to examine some *gross features* of SIMON -calculated heavy-ion collisions, and to examine some *sensitivities* of these features to variations in the SIMON models.

We shall occasionally refer to "simple SIMON" instead of just "SIMON," so as to emphasize that we are using simplified assumptions within a framework that is capable of incorporating more realistic features.

There is one many-body problem for which our simple SIMON code calculates exact results (exact except for machine roundoff). This is the case of a nucleus-nucleus collision in which every nucleon is modeled as a classical frictionless billiard ball, i.e., as a "hard sphere." A fluid-dynamic code could solve the same problem approximately, by using the equation of state and transport properties of a hard-sphere gas. Then a comparison between SIMON results and fluid-dynamic results could teach us something about the effects introduced by the instantaneous local equilibrium assumed in fluid-dynamic approaches. A many-body billiard-ball model is one of the several different SIMON models used in this paper.

Section II describes our SIMON models. Section III reports density patterns $\rho(\vec{r}, t)$. Section IV reports scattered-particle yields $d^2n/dE\,d\Omega$. Section V contains a summary.

II. SIMON MODELS AND METHODS

The basic scheme of the SIMON computer code has been described previously.[27,28] Although we repeat a bit of the old material here, we emphasize new considerations and describe some additional SIMON options for the *NN* interaction. Also, as a way of supporting our SIMON approximations, we compare some recent experimental data with results from a SIMON calculation reported several years ago.

In simulating a ^{20}Ne + ^{238}U collision, SIMON computes classical trajectories for all 258 nucleons.

The trajectories are determined by initial conditions and by *NN* interactions. For these conditions and interactions we have used several alternative SIMON models, differing from each other principally in the size of the nucleonic hard core and in the magnitude of the *NN* cross section. Although we do not regard the detailed nucleon trajectories as realistic, we do expect that gross statistical features of the *NN* energy exchanges, of *NN* momentum exchanges, and of mass transport will be realistic. Because we are interested in gross statistical features, we compute *ensemble averages* of the results from many separately simulated ^{20}Ne + ^{238}U collisions.

Below, subsection A describes a model which treats every nucleon as a classical frictionless billiard ball. Subsections B and C explain how our other alternatives resemble this billiard-ball model, and differ from it. Subsection D considers ensemble averaging—in particular, ensemble averaging *after* simulating many heavy-ion collisions, rather than *while* simulating a heavy-ion collision.

A. The many-body billiard-ball model

Consider ^{20}Ne modeled as a collection of 20 billiard balls, striking ^{238}U similarly modeled as 238 billiard balls. All these billiard-ball nucleons are assumed to be perfectly smooth (i.e., frictionless), all are assumed to have the same mass, and all are treated in classical nonrelativistic mechanics. Each is taken to have diameter 0.9 fm. The resulting cross section σ_{NN} is all elastic and isotropic, with magnitude 25.4 mb. Arguments defending this simple cross section (and defending our other approximations) will be presented shortly. We neglect nuclear binding forces, and we neglect internal kinetic energy of the precollision nuclei.

In this billiard-ball model the course of any single ^{20}Ne + ^{238}U collision is determined completely once we specify the initial positions and velocities of all 258 nucleons. For each of the two precollision nuclei A we consider a sharp-edged nuclear "probability sphere" of radius $1.16A^{1/3}$ fm. We take the precollision positions and velocities of these spheres to be consistent with the nucleus-nucleus vector impact parameter $\vec{b}_{NeU}$, and with the incident beam energy per nucleon $(E/A)^{\rm LAB}_{\rm BEAM}$. Then within each nucleus we choose initial positions for the A nucleon centers at random, assuming that within each of the sharp-edged spheres the probability density for nucleons is uniform and uncorrelated except for the requirement that no two billiard balls overlap. For the initial nucleon velocities we do not use any random numbers, for, as mentioned previously, we neglect the initial internal kinetic energies of both ^{20}Ne and ^{238}U. Thus initially every nucleon has the precollision velocity of its native probability sphere ^{20}Ne or ^{238}U.

Next we discuss the goodness of some of the physical approximations described above. Their goodness depends, of course, on what kinds of calculated results one considers (e.g., on which velocity regions one considers for nucleons emerging from the heavy-ion collision).

Our billiard-ball cross section σ_{NN} is all elastic and isotropic, with magnitude 25.4 mb. This is roughly realistic for *NN* interactions at relative energies 200–400 MeV, except for the experimentally observed[35] forward and backward peaking. To see this, refer to Fig. 1 and realize that in SIMON we should use "classical" cross sections which count only scattered incident particles, and which for *pp* and *nn* correspond to half the cross sections plotted in Fig. 1. Thus as Fig. 1 shows, in the *NN* c.m. system, in the angular region away from the forward and backward peaks, the differential *NN* cross section that is appropriate for SIMON is about 2 mb/sr, i.e., about $25/4\pi$ mb/sr. In other words, $\sigma_{NN} = 25.4$ mb is a reasonable choice provided that it is reasonable to ignore the nuclear (and Coulomb) forward and backward peaks. Below, we give some rough arguments indicating why these peaks are not so important for our purposes.

When all model nucleons are considered identical, exactly forward (0°) and exactly backward (180°) elastic scattering each leave the partici-

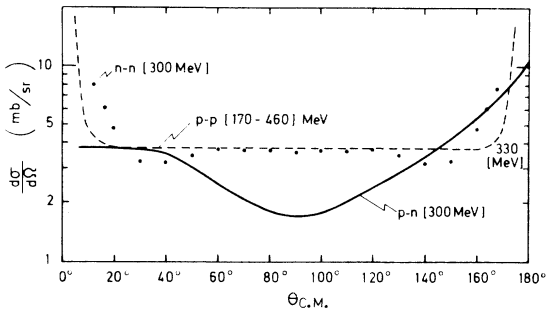

FIG. 1. Experimentally determined nuclear (non-Coulomb) elastic *NN* cross sections, for laboratory energies as marked (Ref. 35). For $ij = nn$ or pp or pn, the plotted cross section counts all emergent particles of type i, not distinguishing between identically charged projectile and target nucleons. This drawing of experimental elastic cross sections has been published previously, in Ref. 27. For some estimates of nonelastic effects see Ref. 36. There it is estimated that in ^{20}Ne + ^{238}U collisions the effective (Fermi-motion-smeared) cross section $\sigma(pp \to pn\pi^+)$ is about 0.6 and 3 mb at $(E/A)^{\rm LAB}_{\rm BEAM} = 250$ and 400 MeV, respectively.

pating NN pair with exactly the same two momenta as before the scattering. Thus when we neglect some *near*-forward and *near*-backward scattering, we are neglecting scatterings which leave NN pairs with *almost* the same two momenta as they had before scattering. However, we are still including those NN scatterings which are most important for effecting large changes in the transverse momenta of two approaching nucleons, and so most important for thermalizing the collided matter during a heavy-ion reaction. This emphasis on "thermalizing" scatterings is a bias familiar from the way that Bodmer and collaborators[30,31] choose NN c.m. cross sections to use in classical equations-of-motion calculations of heavy-ion collisions. Bodmer *et al.* concentrate on fitting the 90°-emphasizing moment $\sigma^{(2)} \equiv \int_{4\pi} (1 - \cos^2\theta)(d\sigma/d\Omega)d\Omega$, rather than on fitting the total NN cross section. In line with our emphasis on thermalizing collided matter, when we examine nucleon-matter velocity distributions at the end of the modeled ^{20}Ne + ^{238}U collision, we pay attention to much of the spectrum but do not take seriously any details in velocity regions near the initial ^{20}Ne and ^{238}U velocities.

These last-mentioned velocity regions tend to be somewhat unreliable anyway, for some additional reasons—our neglect of nuclear binding forces, and our neglect of the internal kinetic energy of both precollision nuclei. In some ways these two simplifications tend to compensate for each other. In both the precollision system and the collided-matter system, binding forces influence nucleons to stay together. Initial internal kinetic energy, whether by itself or after combination with heat produced by the heavy-ion collision, influences nucleons to disperse from each other. By neglecting both binding forces and initial internal kinetic energy, we avoid either collapse or disintegration of the initial projectile and the initial target. Also, we avoid the expense of computing many inconsequential NN scatterings, i.e., those involving nucleons not yet perturbed by the collision of Ne-projectile matter with U-target matter. After the precollision stage, the high energy of the ^{20}Ne + ^{238}U collision helps to excuse our neglect of both binding forces and initial internal kinetic energy. Thus in real nuclei, *one* manifestation of the combined effect of binding potential and internal kinetic energy is the nuclear binding energy; and for the beam energies we consider, the binding energy per nucleon is much less than the precollision kinetic energy of a typical nucleon inside Ne relative to a typical nucleon inside U. (Of course, simple energy comparisons do not tell the whole story. A more thorough discussion would involve vector additions of initial Fermi-motion velocities with beam velocity, etc.)

Because simple SIMON neglects binding, all nucleons which scatter at least once become part of the calculated emitted-nucleon spectrum. Some of the low-energy emitted nucleons should be reinterpreted as belonging to residual heavy fragments, but we do not know which ones should be so reinterpreted. Therefore, besides withholding attention from emitted yields at velocities near the original ^{20}Ne and ^{238}U velocities, we avoid consideration of total emergent-nucleon cross sections (those calculated by integrating over all energies of emergent nucleons).

For a modification to the above discussion of SIMON's approximations, see Ref. 66. For extensions, see the next subsection.

B. Features common to all our SIMON models

For other SIMON models used in this paper, we depart from the billiard-ball option but still keep many of its simplicities. We always use classical nonrelativistic kinematics. We assume that each nucleon travels on a continuous path, with constant velocity except for an abrupt change each time it scatters with another nucleon. We neglect the Pauli principle, nuclear binding, Coulomb effects, and internal kinetic energy of the precollision nuclei. We ignore pion production, velocity-dependent interactions, and all other effects inconsistent with σ_{NN} being purely elastic, isotropic, and independent of the initial NN state.

All these simplifications make the computed history of each ^{20}Ne + ^{238}U collision completely independent of the incident beam speed v_{NeU}, except for the rate at which the history proceeds. For example, doubling the initial beam velocity $\vec{v}_{NeU}$ doubles all computed nuclear velocities at any stage of the reaction. This scaling property makes it appropriate to report SIMON results using velocity units proportional to v_{NeU}, energy units proportional to the beam energy per nucleon $(E/A)^{\rm LAB}_{\rm BEAM}$, etc.

To the extent that different SIMON models involve similar simplifying assumptions, the billiard-ball model and our other SIMON models deserve similar criticisms and similar defenses. For discussion relevant to the *a priori* goodness of SIMON's assumptions, see Sec. II A and the literature.[27,6,30,36,37] As to *a posteriori* evaluation, we consider here some results from a SIMON billiard-ball calculation reported several years ago. Figure 2 displays these old billiard-ball results[38] (black dots), in comparison with recent experimental data[39] (dashed and solid lines) for nucleon charges emitted from ^{20}Ne + ^{238}U reactions.[40] In Fig. 2 we do not use ordinary energy units such as MeV. Instead, in order to compare

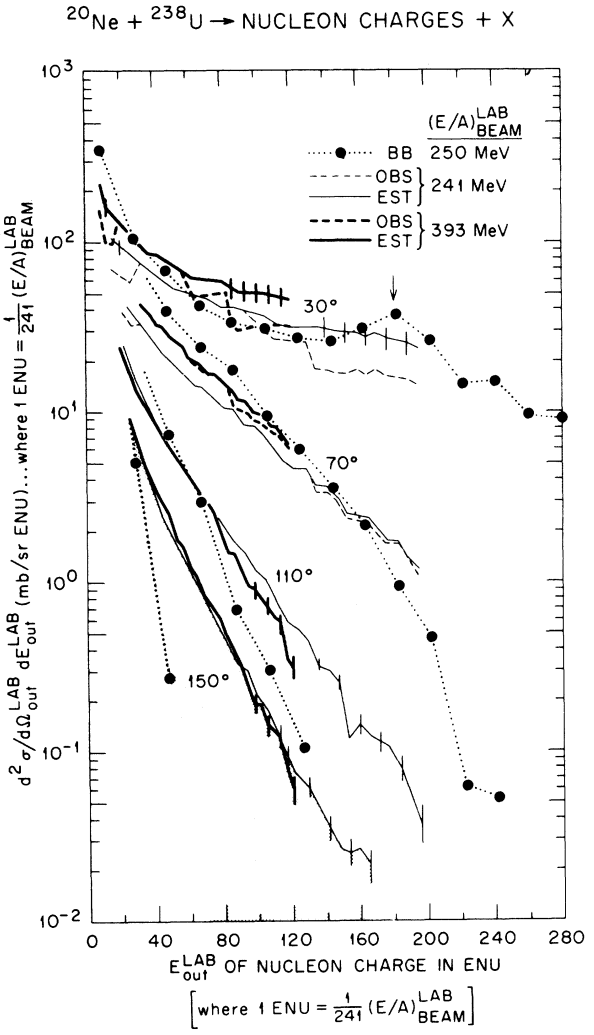

FIG. 2. Experimental and theoretical results plotted using energy units ENU, where 1 ENU = $\frac{1}{241}$ $(E/A)^{LAB}_{BEAM}$. Here SIMON 's billiard-ball model results (BB) are compared with the OBS (observed) and EST (estimated) results deduced by Sandoval *et al.* from their experimental data (Ref. 39). Where a solid line overlays a dashed line, the OBS and EST results essentially coincide. All the results are for inclusive double-differential cross sections describing emission of nucleon charges from the reaction $^{20}Ne + ^{238}U$. The energy units ENU are chosen proportional to $(E/A)^{LAB}_{BEAM}$, the laboratory beam energy per nucleon, because such a choice for energy units makes the BB results independent of $(E/A)^{LAB}_{BEAM}$. Some sample statistical-uncertainty bars are shown for the EST data, but only in those regions where the bar lengths exceed the diameter of the circle symbols marking BB points. In addition to the statistical uncertainties in the EST data, there is an uncertainty of ±20% in the absolute normalization. Where a displayed BB curve stops short of the right axis, its next point (and most succeeding points) would correspond to zero calculated yield (i.e., no counts in the bin).

simultaneously with the experimentally determined data at two different beam energies—$(E/A)^{LAB}_{BEAM}$ = 241 and 393 MeV—we have plotted Fig. 2 using energy units proportional to $(E/A)^{LAB}_{BEAM}$. When units with this proportionality feature are used, simple SIMON 's results are independent of the initial bombarding energy. (See the preceding paragraph.) The energy units used in Fig. 2 are called ENU; and they are defined by 1 ENU = $\frac{1}{241}(E/A)^{LAB}_{BEAM}$, so that 1 ENU is 1 MeV when $(E/A)^{LAB}_{BEAM}$ = 241 MeV. Therefore in Fig. 2 the experimental data can be considered as plotted in the usual way for $(E/A)^{LAB}_{BEAM}$ = 241 MeV, but plotted in a rescaled way for $(E/A)^{LAB}_{BEAM}$ = 393 MeV.

As Fig. 2 shows, simple SIMON reproduces the major measured trends in energy and angle dependence. The most prominent deviations occur in the energy-angle regions of smallest cross section.

Before discussing Fig. 2 much further, we stress again that in this paper our main concern is not the close reproduction of measured data. Rather, our main concerns are to examine some gross features of SIMON-calculated heavy-ion collisions, and to examine some sensitivities of these features to variations in the SIMON models. Figure 2 has been included mainly as evidence that our billiard-ball model, and other SIMON models which resemble it, are roughly realistic. Since this point is conveyed without a detailed discussion of Fig. 2, we relegate most further analysis of this figure to Appendix A. However, two features of Fig. 2 merit some attention here in the main text: (a) one particular rescaling feature, and (b) the arrow at $\theta^{LAB}_{out} = 30°$.

(a) Figure 2 shows a close match between the experimental data sets at $(E/A)^{LAB}_{BEAM}$ = 241 and 393 MeV (light and heavy curves, respectively). That nice match would suffer greatly if we were to drop the rescaling device and so replace our ENU plot with a simple MeV plot. In particular, suppose we were to keep all the numerals on the vertical and horizontal scales as now shown, change their meaning to involve MeV (instead of ENU), and then replot accordingly. The experimental curves for $(E/A)^{LAB}_{BEAM}$ = 241 MeV would remain exactly as now shown; but every point of the experimental curves for $(E/A)^{LAB}_{BEAM}$ = 393 MeV would change both in vertical and horizontal position. These 393-MeV curves would be stretched out to larger numerical values of E^{LAB}_{out}. That is, on our ENU plot of Fig. 2 the experimental data sets for $(E/A)^{LAB}_{BEAM}$ = 241 and 393 MeV extend to $E^{LAB}_{out} \approx 195$ and 120 ENU, respectively; but on an unrescaled MeV plot both of these data sets would extend to ≈195 MeV. The other prominent change would be, qualitatively, like an upward rotation of the 393-MeV experimental curves around a fulcrum at low

E_{out}^{LAB} ($\lesssim$20 on the horizontal scale). On the resulting MeV plot: For the case $\theta_{out}^{LAB}=70°$, the 393-MeV data would lie higher than the 241-MeV data by factors of about 1.6, 2.1, and 3.2 at $E_{out}^{LAB}=80$, 120, and 195 MeV, respectively. For $\theta_{out}^{LAB}=110°$, these discrepancy factors would be about 1.8, 2.8, and 5.1 at $E_{out}^{LAB}=80$, 120, and 195 MeV, respectively. For $\theta_{out}^{LAB}=150°$, these discrepancy factors would be about 3.2, 5.5, and 5.6 at $E_{out}^{LAB}=80$, 120, and 165 MeV. For the smallest angle shown, $\theta_{out}^{LAB}=30°$, a conventional MeV plot would show somewhat closer agreement between the 241- and 393-MeV data sets than is shown in our ENU plot of Fig. 2. But for this angle, on either the ENU plot or an MeV plot, the discrepancy between the 393-MeV EST data and the 241-MeV EST data (where EST implies estimated) is $\leq$ the difference between the two 393-MeV data sets [EST and OBS (observed)] that were deduced by the experimentalists from their measurements.

(b) Now we explain the arrow in Fig. 2. Though shown here in connection with SIMON billiard-ball results, arrows of this kind are relevant to results from all our SIMON models. As Fig. 2 shows, at $\theta_{out}^{LAB}=30°$ our SIMON curve has a relative peak in the region of emitted-particle energy $E_{out}^{LAB}=183$ ENU. We interpret this peak as caused by particles emitted after "first scattering," where by first scattering we mean the SIMON scattering of a previously unperturbed projectile nucleon with a previously unperturbed target nucleon. Because we ignore internal kinetic energy in the precollision projectile and target, and because we conserve linear momentum and translational kinetic energy, particles emitted after first scattering are restricted to a pure one-to-one correspondence $\{E_{out}^{LAB}, \theta_{out}^{LAB}\}$. This one-to-one correspondence is given by

$$E_{out}^{LAB}=\tfrac{1}{2}(E/A)_{BEAM}^{LAB}(1+\cos 2\theta_{out}^{LAB}) \quad \text{for first scattering.} \tag{1}$$

This relation (1) is not peculiar to the billiard-ball model; it is the same for all our present SIMON results, because they all begin with classically cold precollision nuclei and they all conserve linear momentum and translational kinetic energy. The small arrow in Fig. 2, which appears near the 30° curve, indicates the first-scattering pair $\{E_{out}^{LAB}, \theta_{out}^{LAB}\}$ having $\theta_{out}^{LAB}=30°$. In our SIMON results of Fig. 2, the one-to-one first-scattering correspondence $\{E_{out}^{LAB}, \theta_{out}^{LAB}\}$ is effectively broadened because of the nonzero widths of the energy-angle bins used in converting discrete-particle information to a double-differential distribution. (See Appendix A.) In a real $^{20}Ne+^{238}U$ reaction, precollision Fermi motion *also* broadens the one-to-one correspondence $\{E_{out}^{LAB}, \theta_{out}^{LAB}\}$. Broadening tends to wash out the peaks. However, the 30° experimentally determined curves in Fig. 2 do seem to show, in the region of $E_{out}^{LAB}\approx 180$ ENU, some lifting of the downward slope. This suggests that first scatterings may have a non-negligible effect in shaping the real energy-angle distribution. For $\theta_{out}^{LAB}=70°$ in Fig. 2, the first-scattering arrow would appear at $E_{out}^{LAB}=28$ ENU. (See Appendix A.) Beyond 90° there are no first-scattering combinations $\{E_{out}^{LAB}, \theta_{out}^{LAB}\}$.

Figure 3 is like Fig. 2 but shows the double-differential cross sections versus angle instead of energy. Again we see that simple SIMON reproduces the main trends of the experimentally determined results, deviating most prominently in the regions of smallest cross sections, i.e., at large angles toward high energies. For all three energies shown in Fig. 3, the SIMON BB model yields discernible peaks near the energy-angle pairs indicated by first-scattering arrows. For further discussion see Appendix A.

C. Differences among four *NN* scattering styles

Why have we tried *NN* scattering mechanisms other than the billiard-ball model? Our main reason is that the excluded-volume aspect of the billiard-ball model seems unsatisfactory. To get a realistic *NN* cross section ($\sigma_{NN}\approx 25$ mb) we must use billiard balls of diameter $\approx$0.9 fm, but this diameter restricts nucleon centers to be much further apart than the minimum of $\approx$0.5 fm imposed by the hard-core radius of a typical realistic *NN* potential. The discrepancy becomes worse yet if we continue to use the billiard-ball model while exploring the effects of yet larger σ_{NN}. However, by departing from the billiard-ball mechanism we can divorce the choice of σ_{NN} from the choice of excluded volume.

Below, we list four *NN* scattering mechanisms, i.e., four "styles." In describing them we denote by $\Omega_{NN}^{c.m.}=(\theta_{NN}^{c.m.}, \phi_{NN}^{c.m.})$ the scattering angles in the *NN* c.m. system. (The polar angle $\theta_{NN}^{c.m.}$ is measured with respect to the direction of the *NN* relative velocity.) We have, in order of decreasing excluded volume:

(1) BB, meaning billiard-ball scattering, with balls of diameter 0.9 fm.

(2) RC, meaning repulsive in-plane impact scattering with billiard-ball core. Here if two approaching nucleons have impact parameter $b_{NN}\leq(\sigma_{NN}/\pi)^{1/2}$, they scatter as soon as their separation decreases to b_{NN} or to 0.5 fm, whichever happens first. If $b_{NN}\leq 0.5$ fm then the scattering is computed as if two billiard balls, each of diameter 0.5 fm, were scattering from each other. If $0.5\text{ fm}<b_{NN}\leq(\sigma_{NN}/\pi)^{1/2}$, then $\phi_{NN}^{c.m.}$ is chosen to

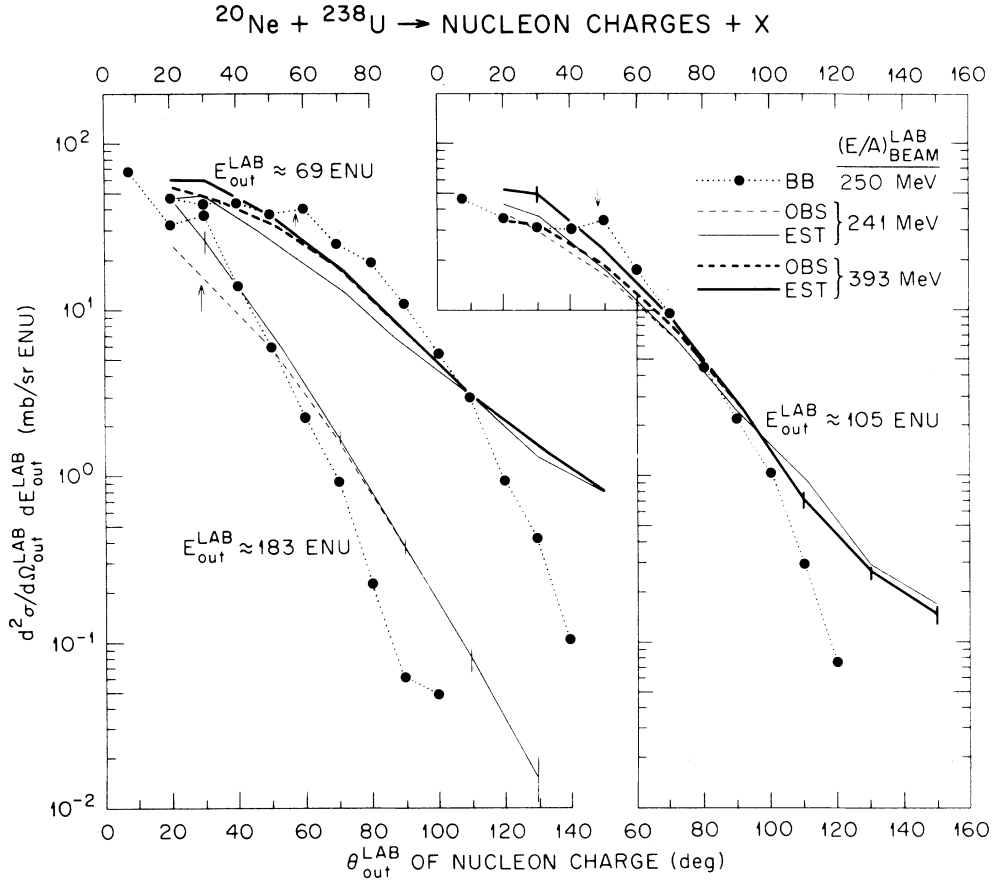

FIG. 3. Same as Fig. 2, but plotted versus angle instead of energy. As in Fig. 2, the thin and thick lines refer, respectively, to experimentally determined results at $(E/A)_{BEAM}^{LAB} = 241$ and 393 MeV. Each curve has an assigned (median) energy E_{out}^{LAB} that is within 2 ENU of its label (69, 105, or 183 ENU). For $E_{out}^{LAB} \approx 183$ ENU there are no experimental points from $(E/A)_{BEAM}^{LAB} \approx 393$ MeV because the experimental information stops at a considerably lower E_{out}^{LAB}.

give repulsive[41] in-plane scattering, while $\theta_{NN}^{c.m.}$ is chosen randomly assuming uniform distribution of $\cos\theta_{NN}^{c.m.}$ within the interval $[-1, 1]$.

(3) RN, meaning repulsive in-plane scattering with no core. This is the same as RC except that the billiard-ball core is absent (shrunk to zero size).

(4) 4πI, meaning 4π impact scattering. Here if two approaching nucleons have impact parameter $b_{NN} \leq (\sigma_{NN}/\pi)^{1/2}$ they scatter as soon as their separation decreases to b_{NN}, and then the scattering angle $\Omega_{c.m.}^{NN}$ is chosen randomly assuming uniform distribution within the entire solid angle of magnitude 4π. Note that this style allows attractive[42] as well as repulsive[41] scattering. Just after an attractive NN scattering, the two scattered nucleons are again approaching each other, and the new impact parameter will again be $\leq (\sigma_{NN}/\pi)^{1/2}$. However, we avoid multiple sequential scatterings of the same nucleon pair by imposing an extra restriction—that if two nucleons have once scattered with each other they do not rescatter with each other until at least one member of the pair has scattered with a different partner.

The post-scattering nucleon speeds are always determined by requiring conservation of linear momentum and translational kinetic energy within each NN event. Style BB conserves angular momentum too, within each NN event.[43]

Style BB allows nucleon-nucleon separations ≥ 0.9 fm, RC allows ≥ 0.5 fm, and RN and 4πI each allow any separation ≥ 0 fm. In choosing initial conditions we impose these same minimum NN separations, except that for RN we require every initial separation to be ≥ 0.5 fm even though this restriction ceases to apply after the collision begins.

When using a given NN scattering style, we must restrict ourselves to cross sections σ_{NN} such that the interaction range $(\sigma_{NN}/\pi)^{1/2}$ is $\geq$ the minimum allowed nucleon-nucleon separation. For BB and RN we have used only the interaction range 0.9 fm, implying $\sigma_{NN} = 25.4$ mb. For each of RC and

4πI we have performed calculations using interaction ranges 0.7, 0.9, and 1.3 fm, implying $\sigma_{NN} = 15.4$, 25.4, and 53.1 mb, respectively.

For σ_{NN} fixed at 25.4 mb, the differences among BB, RC, and RN are in their excluded-volume aspects. Style 4πI stands somewhat apart from the trio BB, RC, and RN because 4πI allows out-of-plane scattering and attractive scattering, as well as repulsive in-plane scattering. Style 4πI is the only one, among our four, which allows the *NN* distance of closest approach to be smaller than the impact parameter b_{NN}. The general lack of constraints on 4πI make scatterings in this style close in character to those in most conventional[34] Monte Carlo cascade calculations.

D. Ensemble averaging

For all our *NN* scattering models, we compute statistical aspects of ^{20}Ne + ^{238}U collisions by taking *ensemble averages* over the results calculated from many different simulated collisions. For example, we report ensemble-averaged density patterns $\rho(\vec{r}, t)$.

An ensemble consists of many computed ^{20}Ne + ^{238}U collisions all identical in their gross initial conditions and *NN* scattering rules, i.e., all identical in $\vec{v}_{NeU}$, in the initial positions of their probability spheres, in scattering style, and in σ_{NN}. The differences of detail, from one collision to another within an ensemble, are caused by differences among the ordered sets of random numbers which help to determine the nucleon trajectories. In our billiard-ball model BB, each collision-history proceeds deterministically once the initial nucleon positions are set. Therefore in style BB all differences among collisions are due to differences in the initial random placement of nucleons, within the fixed-position initial probability spheres. In our other SIMON models there are further sources of differences, because in these other models, random-number choices help to determine not only the initial nucleon positions but also the *NN* scattering angles $\Omega_{NN}^{c.m.}$.

All the numerical results reported in this paper were calculated using the ensemble sizes shown in Table I. (Computing time is mentioned in a footnote there.)

For results like $d^2n_p/dE_p d\Omega_p$, the final double-differential proton yield per ^{20}Ne + ^{238}U collision, there is little difficulty about the interpretation of an ensemble average; for, aside from the restriction to a fixed value of the ^{20}Ne + ^{238}U impact parameter, $d^2n_p/dE_p d\Omega_p$ is quite analogous to an experimentally determined inclusive energy-angle distribution of "singles." In the case of nucleon density, the idea of an ensemble average is less familiar. Each of our ensemble-averaged density functions $\rho(\vec{r}, t)$ should be interpreted as an approximation to a function $\rho_g(\vec{r}, t)$ indicating *expectation values;* and such an expectation-value function may or may not typify the nucleon-density pattern developed in a *single* ^{20}Ne + ^{238}U collision.

Reporting ensemble averages means reporting inaccurate, incomplete information. We say inaccurate because when we use finite ensembles, we get mean values which are subject to statistical uncertainty. We say incomplete because when we report only ensemble averages, we are suppressing information on fluctuations and correlations. The suppressed information concerns collision characteristics which, although they may be in principle just as interesting as the reported mean-value characteristics, are presumably described by SIMON less realistically than the reported mean-value characteristics.

However, presenting reports which suppress information about correlations is not the same as calculating collision-histories using a method that suppresses correlations. SIMON, like other many-body methods, does involve nucleon-nucleon correlations while it is computing a heavy-ion

TABLE I. Standard ensemble sizes for various choices of $\{b_{NeU}$, style, $\sigma_{NN}\}$. Except for Figs. 2 and 3, Tables II and III, and Fig. 9, all the SIMON results reported in this paper were calculated using the ensemble sizes listed in column 4. [a-c]

Impact parameter b_{NeU} (fm)	*NN* scattering style	σ_{NN} (mb)	Ensemble size [c]
0	BB	25.4	300
	RC	15.4	200
		25.4	300
		53.1	200
	RN	25.4	300
	4πI	15.4	300
		25.4	300
		53.1	199
5	BB	25.4	300
	RC	25.4	300 [b]
	4πI	25.4	300

[a] The ensemble sizes used for Tables II and III are given in the tables themselves. The ensemble sizes used for Figs. 2 and 3 are the same as those noted in Table II.

[b] 199 for Fig. 9.

[c] An ensemble is a collection of heavy-ion collisions. In one minute of IBM-360/91 CPU time, SIMON simulates about 10 collisions of ^{20}Ne with ^{238}U. The timing varies with such things as b_{NeU}, σ_{NN}, and the detail in which a history of each heavy-ion collision is saved on magnetic tape.

collision. This matter is discussed further in Appendix B, where we compare how various theoretical methods handle fluctuations and correlations while calculating heavy-ion collisions.

III. PARTICLE-DENSITY PATTERNS

The main results of this section are in Figs. 4–10. These are plots of nucleon-matter density functions $\rho(\vec{r}, t)$ at various times t during collisions of $^{20}\mathrm{Ne} + ^{238}\mathrm{U}$. An introduction to these density figures is given in subsection A. The physical results are discussed in subsection B for head-on collisions ($b_{\mathrm{NeU}} = 0$), and in subsection C for off-center collisions ($b_{\mathrm{NeU}} = 5$ fm). Some comparisons with fluid-dynamic results are made in subsection D.

A. Introduction to Figs. 4–10

1. Space and time coordinates

In considering particle-density patterns $\rho(\vec{r}, t)$ we sometimes use cylindrical coordinates $\tilde{r}, z, \phi$ and sometimes use Cartesian coordinates x, y, z. However, we always use a laboratory frame having its origin fixed at the initial position of the U-target center, its z axis in the direction of the initial relative velocity $\vec{v}_{\mathrm{NeU}}$, and its xz plane ($y = \phi = 0$) coincident with the collision plane. We characterize the reaction stage not by specifying the time coordinate t in traditional units, but instead by specifying

$z^{\mathrm{unp}}_{\mathrm{NeU}} \equiv$ the z displacement of the Ne center from the U center, calculated by assuming that both nuclei are unperturbed by the collision. (2)

In effect we are using time units inversely proportional to v_{NeU}. This allows us to report SIMON results for $\rho(\vec{r}, t)$ without specifying the initial beam energy. [See our remarks in Sec. II B about scaling, i.e., using velocity units proportional to v_{NeU}, energy units proportional to $(E/A)^{\mathrm{LAB}}_{\mathrm{BEAM}}$, etc.]

2. Technical problems

Next we discuss why, *quite aside from the physical approximations in our SIMON models*, displayed functions $\rho(\vec{r}, t)$ are only approximate versions of the expectation-value functions we want to know.

First we define expectation-value functions more carefully. During the simulation of a $^{20}\mathrm{Ne} + ^{238}\mathrm{U}$ collision, SIMON computes the position of each nucleon as a continuously traveling point in continuous 3-dimensional space.[27,44] Therefore at fixed time $z^{\mathrm{unp}}_{\mathrm{NeU}}$ within a single SIMON collision, the *directly* calculated density of nucleons is very spiky; it is a sum of 258 delta functions. If we could average these delta-function results over an infinitely large ensemble of collisions, we would get an everywhere-finite *expectation-value* function[45]

$$\rho_{\mathcal{E}}(\vec{r}, z^{\mathrm{unp}}_{\mathrm{NeU}})$$

—a different definite function for each of our model combinations $\{\text{style}, \sigma_{NN}, \vec{b}_{\mathrm{NeU}}\}$. These are the functions whose general features we would like to know; and these are the functions we would like to compare for different combinations $\{\text{style}, \sigma_{NN}, \vec{b}_{\mathrm{NeU}}\}$.

Now we define ρ more carefully. Since we cannot afford to calculate ρ by using an infinite ensemble, we try to approximate $\rho_{\mathcal{E}}$ by simple finite averaging.[46] We average first within noninfinitesimal volume elements of size $\gtrsim 2$ fm,[3] and then further, over a finite ensemble of ≈ 300 similar collisions (see Table I). We do this for a set of 12 time-coordinate values $z^{\mathrm{unp}}_{\mathrm{NeU}}$ during collision. What emerges is a finite array of density values, corresponding to a finite array of mesh points $(\vec{r}, z^{\mathrm{unp}}_{\mathrm{NeU}})_{\mu}$, where $\vec{r}_{\mu}$ is an appropriate volume-averaged vector coordinate characterizing the volume element. Then whenever we convert this finite array of density values to information for a contour diagram,[47] we introduce some interpolation approximations. The finally displayed density functions are called $\rho(\vec{r}, z^{\mathrm{unp}}_{\mathrm{NeU}})$, and they differ from $\rho_{\mathcal{E}}(\vec{r}, z^{\mathrm{unp}}_{\mathrm{NeU}})$ for three reasons:

(a) statistical uncertainty (because we have not calculated ρ using infinitely large ensembles),
(b) nonzero space resolution (because we have not calculated ρ using infinitesimally small volume elements),[48] and
(c) interpolation approximations.

All three items affect $\rho(\vec{r}, z^{\mathrm{unp}}_{\mathrm{NeU}})$ significantly. Therefore we have been concerned with all three items in preparing our figures, captions, and text. In particular: (a) Some quantitative estimates of the statistical uncertainty are presented as error bars in Figs. 8 and 10 ahead. (b) For most of our figures, the space resolution is $\gtrsim 1$ fm and the associated details are given in the captions. (c) In all our plots, contour and other, we have used very simple *linear* interpolations.[47] This linear-interpolation choice is just a small step beyond using histograms, and has the advantage of retaining jagged features which serve as constant reminders of the nonideal statistics and imperfect space resolution.

As an example of how items (a), (b), and (c) affect $\rho(\vec{r}, z^{\mathrm{unp}}_{\mathrm{NeU}})$, consider Fig. 4(a). This is a precollision picture of ρ/ρ_0, where ρ_0 represents normal nuclear density because

$\rho_0 \equiv$ the magnitude of ρ inside our initial probability spheres. (3)

Figure 4(a) shows two rather lumpy diffuse-edged objects, just touching each other. What would Fig. 4(a) show, instead, if we had calculated ρ by using infinitesimally small volume elements, an infinitely large ensemble, and an infinitely refined contour-plotting routine? In that triply ideal case Fig. 4(a) would show $\rho_{\mathcal{E}}$: two sharp-edged spherical nuclei, each of uniform density[49] $\rho/\rho_0 = 1$, with surfaces 1.66 fm apart.[50] This initial discrepancy between ρ and $\rho_{\mathcal{E}}$ conveys an idea of how ρ may differ from $\rho_{\mathcal{E}}$ later during the collision too.

3. *More about* t_{STOP}

There are qualitative differences in meaning between our contour plots of $\rho(\vec{r}, t)$ and some related displays in the literature. In our present paper the plotted contours always refer to nucleons per unit volume. In contrast, some other displays in the literature involve densities integrated along the direction y perpendicular to the collision plane, so that the quantities displayed have units nucleons per unit area. For example, some displays show point-nucleon positions, one dot per nucleon, projected onto the collision plane xz but altered slightly so as to make every nucleon-dot appear separately instead of being shielded by other nucleon dots.[27] Such plots fold together density information and information about the occupied volume's thickness perpendicular to the collision plane; thus for example a uniformly dense sharp-edged sphere would be pictured as a circular area with more nucleons/(unit area) near the center than near the periphery. Turning now to the familiar collision-diagrams of Amsden *et al.*,[16,17] which display fluid-dynamic results, we note these three features: (a) The dots represent projections of computational points (not nucleon positions) onto the collision plane. (b) The precollision pictures show circular areas which are almost uniform in their dots/(unit area) because no antishielding alterations have been made, and because the computational points are initially placed in a rectilinear array leading to much shielding. (c) During nuclear collisions, the diagrams develop crowded regions of dots/(unit area) largely because of displacements ruining the shielding, though partly because of real increases in the points/(unit volume) and associated increases in its projected version, points/(unit area). In short, crowded areas of an Amsden *et al.* plot tend to indicate *disturbed* matter, not necessarily matter dense in nucleons/(unit volume). That is a useful kind of display, but one should realize the difference between that kind of display and the contour diagrams of this paper.

In all our cylindrical contour plots (Figs. 4–7) we show a cylindrically symmetrized function $\rho(\vec{r}, t)$ versus z increasing from left to right, and versus $\bar{r}$ increasing upward. In Fig. 4, in order to make the collision easier to visualize, we have also reflected the $\bar{r} \geq 0$ plot downward through the z axis, so that $\bar{r}$ increases both upward and downward from the $\bar{r} = 0$ line.

In Figs. 4–7 a blank strip appears along each z axis. Its presence is explained briefly in the Fig. 4 caption and more thoroughly in Ref. 51.

B. ρ in head-on collisions

Readers who want to skim this subsection will find its main points in paragraphs which begin with an italicized word.

Figure 4 pictures the general course of a head-on $^{20}\mathrm{Ne} + {}^{238}\mathrm{U}$ collision. At each time stage, a five-pointed star shows where the center of an unperturbed Ne projectile would be. High densities ($\rho/\rho_0 \gtrsim 2$) develop soon after geometric contact is made; then the near (struck) side of the U target becomes blasted away, leaving a crescent-shaped pattern. In the interior of the crescent, ρ decreases gradually with time. On the far side of the target there is a front of low density which moves slowly outward into previously unoccupied space. There are no signs of a discrete fireball or a residual projectile. (The term "crescent" may be slightly misleading. The contours plotted in $\bar{r}, z$ space really imply the 3-dimensional contours that would be generated by rotation around the z axis.)

At all of the collision stages shown in Figs. 4(b)–4(e), the highest-density region is in the interior near the collision axis, and it tends to lag behind the star-marked point where the center of an unperturbed Ne projectile would be. This kind of lag is consistent with the behavior of a shocklike zone, which would have shock-front speed slower than the speed of unperturbed projectile matter.

Figure 4 demonstrates how, at any stage of the collision, one can tell just from the density pattern which regions of our model nuclei have already been perturbed significantly. Recall that we neglect internal kinetic energy within both precollision nuclei. Consequently at any point $\bar{r}, z$ statistical fluctuations in the initial density pattern persist with time until the nucleus-nucleus collision causes nucleons to move to or from that $\bar{r}, z$. Note for example that in Fig. 4(b) there is not yet any disturbance of the initial fluctuation evident between $z = 1$ and $z = 2$ at small $\bar{r}$; and in Fig.

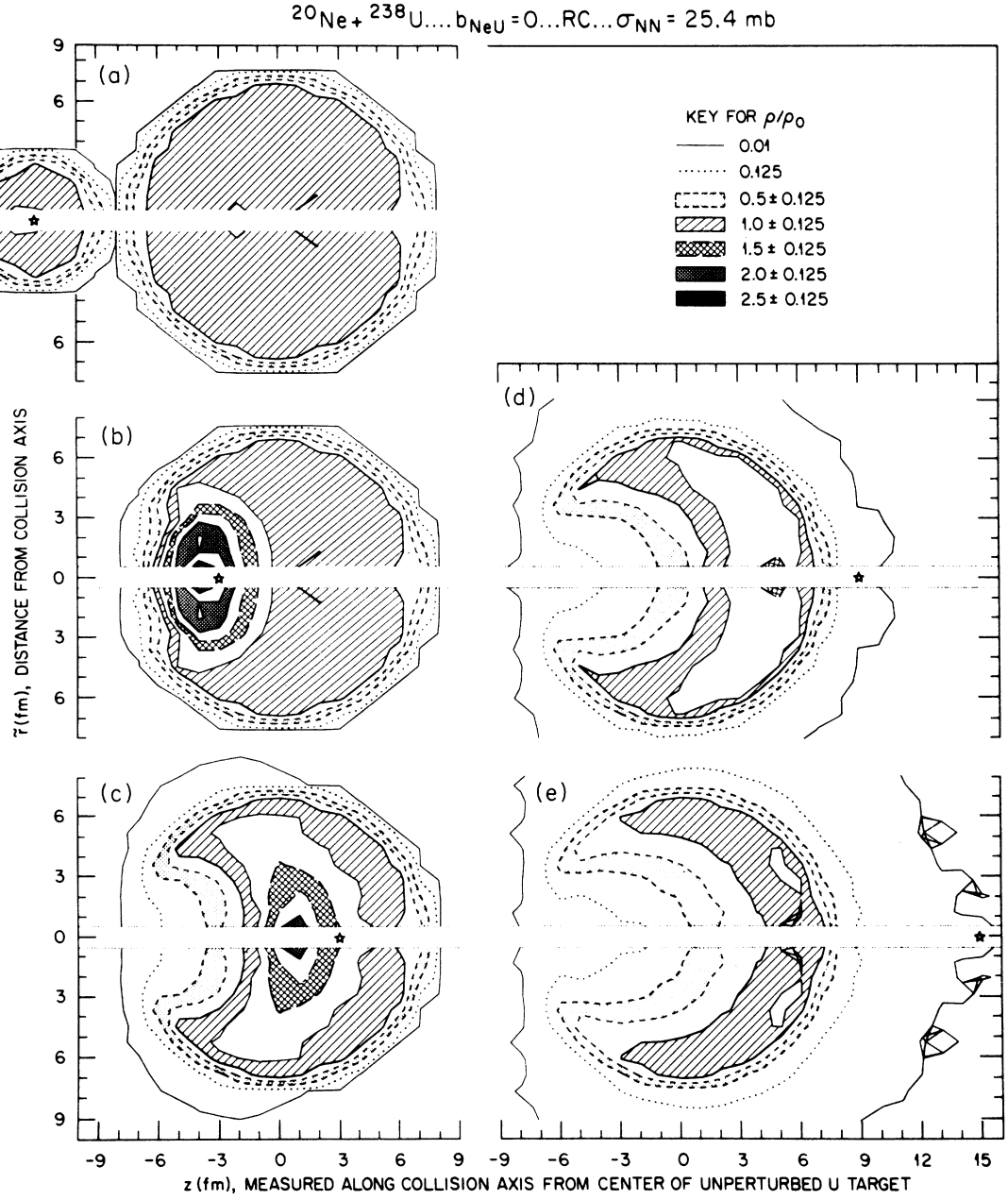

FIG. 4. Contour plots showing time development of the nucleon-matter density ratio ρ/ρ_0 during head-on collision of ^{20}Ne with ^{238}U. Each five-pointed star indicates time by showing where the center of an unperturbed Ne projectile would be. The densities ρ are obtained by averaging first within small finite volume elements, and then further over an ensemble of several hundred collisions (see Table I). Cylindrical coordinates $\tilde{r}$, z, and ϕ are used; and the space resolution is $\lesssim 1$ fm because the volume elements are contiguous discs and rings each of dimension $\Delta\tilde{r} = 0.8$ fm, $\Delta z = 1.0$ fm, and $\Delta\phi = 2\pi$. The area keyed $(\rho/\rho_0) = 0.5 \pm 0.125$ is bounded by contour lines for 0.375 and 0.625, and similarly for the other keyed areas. Thus, in general, blank areas imply regions where ρ/ρ_0 could be estimated by interpolation. An exception is the no-interpolation blank strip along each z axis; there ρ/ρ_0 could be estimated by extrapolation but not by interpolation. For further explanation see the text of Secs. III. A and III. B.

4(c) there is still no disturbance of the initial bumps at $z \geq 0$ in the contour $\rho/\rho_0 = 0.875$ that forms the outer boundary of the diagonally striped region $\rho/\rho_0 = 1.0 \pm 0.125$.[52]

Figure 5 is the first picture indicating how $\rho(\vec{r}, z^{\text{unp}}_{\text{NeU}})$ is affected by scattering style and σ_{NN}. In Fig. 4, we showed time-sequenced information for a *single* combination {style, σ_{NN}}—a combina-

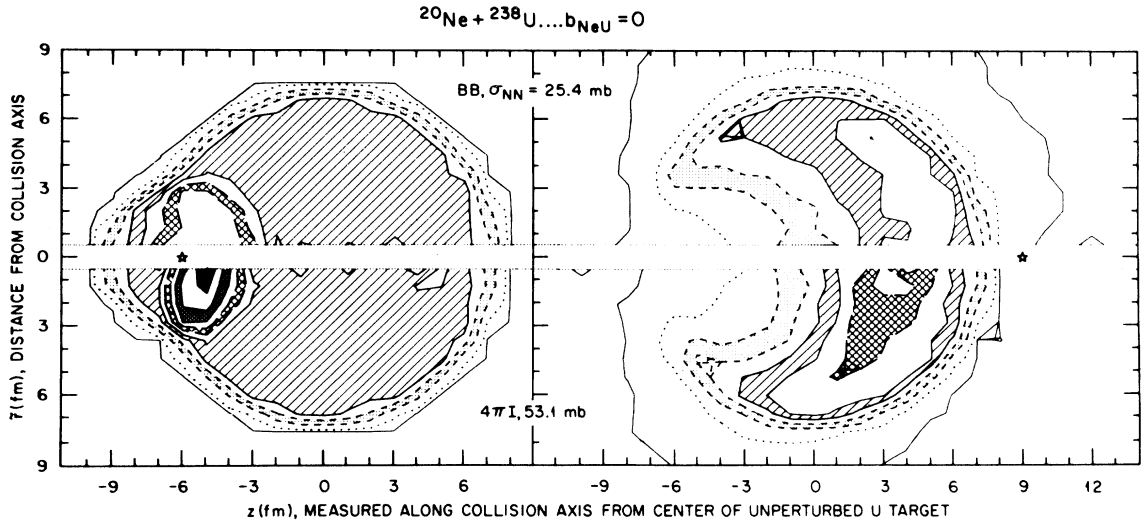

FIG. 5. Contour plots contrasting nucleon-matter densities calculated from two different NN scattering models: BB, 25.4 (upper) and 4πI, 53.1 (lower). The contrast is shown for both an early stage (left) and a late stage (right) during head-on collision of ^{20}Ne with ^{238}U. The key for ρ/ρ_0 is the same as that pictured in Fig. 4. For other conventions see the caption to Fig. 4 and the text of Secs. III. A and III. B.

tion of intermediate character, {RC, 25.4 mb}. Now in Fig. 5 we juxtapose, for each of two times during the ^{20}Ne + ^{238}U collision, a section above the z axis corresponding to {BB, 25.4} and a section below the z axis corresponding to {4πI, 53.1}. Figure 5 shows that the calculated density pattern is indeed sensitive to the combination {style, σ_{NN}}. There is a sensitivity both early in the collision ($z^{\text{up}}_{\text{NeU}} = -6$ fm), and late ($z^{\text{up}}_{\text{NeU}} = +9$ fm). Higher densities are calculated for {4πI, 53.1} than for {BB, 25.4}. This is consistent with the fact that shocklike behavior is more likely to be produced by short-range strong NN interactions than by longer-range weak NN interactions. (Or, to comment more simply, large hard cores inhibit the development of high densities.) Note that at the early stage shown at the left in Fig. 5, model {BB 25.4} does not produce even the overlap compression $\rho/\rho_0 = 2$ (in fact, not even 1.875). In contrast, {4πI, 53.1} produces compressions $\approx$2.5.

As Fig. 5 indicates, the sensitivity to {style, σ_{NN}} is concentrated in the interior region where high density exists. There is an apparent "healing," i.e., insensitivity to {style, σ_{NN}}, near the surface region in which $0.875 \geq (\rho/\rho_0) \geq 0.125$.

The very early stage $z^{\text{up}}_{\text{NeU}} = -6$ fm, shown at left in Fig. 5, is prior to any of the perturbed stages shown in Figs. 4(b)–4(e). This early stage has one feature that is slightly different from what we saw in Figs. 4(b)–4(e), viz., the highest-density region *leads* (rather than lags behind) the star-marked point where the center of an unperturbed Ne projectile would be. This happens because the Ne projectile has radius 3.15 fm and its front edge causes the earliest perturbation of the target. Thus at the very early state $z^{\text{up}}_{\text{NeU}} = -6$ fm in Fig. 5, the highest-density zone does trail behind the place where the *front edge* of an unperturbed Ne projectile would be. However, not enough time has elapsed for the lag to develop so much that the highest-density zone trails behind the place where the *center* of an unperturbed Ne projectile would be.

Note that in the early-stage diagrams of Figs. 4 and 5, within the still undisturbed region where $\rho/\rho_0 \approx 1$ (diagonal-line pattern), the statistical fluctuations are particularly severe near the collision axis z. This is typical; it happens because in our cylindrical volume-element set (see the caption to Fig. 4), the elements near the z axis are especially small and so they tend to hold rather few nucleons and give poor statistics.

Figure 6 shows density results for four different NN-scattering styles but fixed σ_{NN}. All four pictures are for the same stage of the collision: $z^{\text{up}}_{\text{NeU}} = 0$, when an unperturbed Ne projectile would be centered within the U nucleus. As we look down Fig. 6, from BB toward 4πI, we see higher central densities. Recall that as the NN-scattering style is changed from BB to RC, and then from RC to RN or 4πI, there is a decrease in the size of the hard nucleon core. Figure 6 indicates that this decrease in core size leads to higher compressions ρ/ρ_0. Style RN, which is like RC in some NN features (repulsive in-plane scattering), but like 4πI in other NN features (no hard core during scattering), gives a density pattern in between those from RC and 4πI.

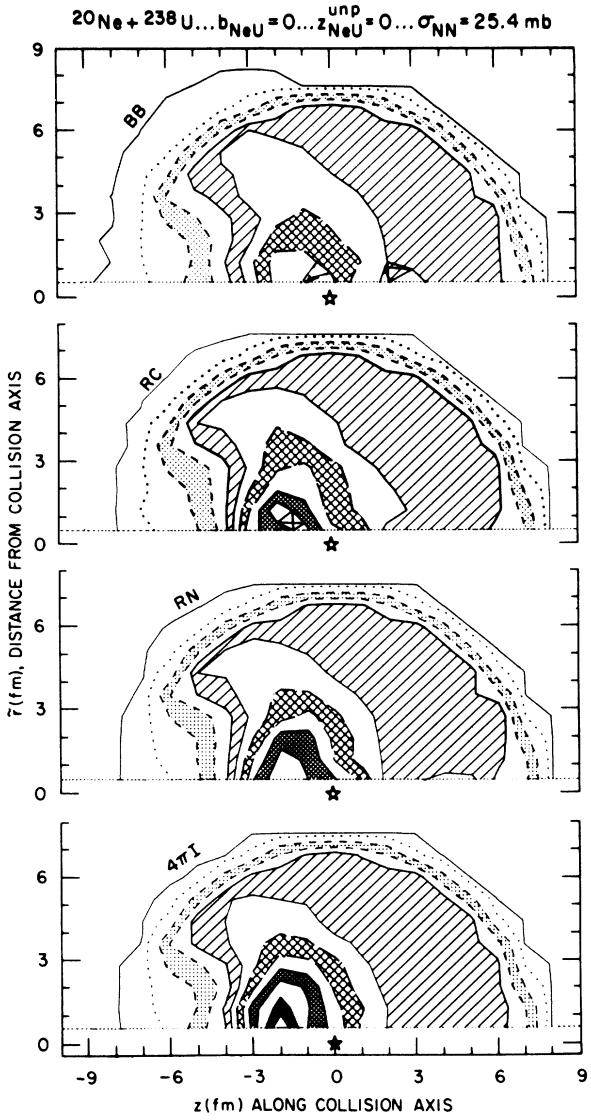

FIG. 6. Contour plots showing nucleon-matter densities calculated by using four different NN scattering styles (BB, RC, RN, and 4πI) all with the same NN cross section (25.4 mb). The comparison is made for head-on $^{20}Ne + ^{238}U$ collision at a time corresponding to $z^{unp}_{Neu} = 0$, i.e., when the projectile center would coincide with the target center if both nuclei were unperturbed. The key for ρ/ρ_0 is the same as that pictured in Fig. 4. For other conventions see the caption to Fig. 4 and the text of Secs. III. A and III. B.

At $z^{unp}_{NeU} = 0$, the time stage shown in Fig. 6, our model U target is almost unperturbed for $z \geq 3$ fm. This is true for all the models in Fig. 6 (and for BB it can be confirmed directly by comparing with the left upper section of Fig. 5).

Figure 7 is a systematic array showing sensitivity both to NN scattering style and to σ_{NN}. The time in Fig. 7 is $z^{unp}_{NeU} \equiv -3$ fm. At this time perturbation is confined to $z \leq 1$ fm and therefore to save space we show only the regions where $z \leq 1$. It is near the time $z^{unp}_{NeU} = -3$ fm that most of our models give their maximum ρ/ρ_0. (This can be verified, for some models, by comparing analogous sections of Figs. 4–7, i.e., sections which show results from the same {style, σ_{NN}} at different times z^{unp}_{NeU}.) Figure 7 confirms, for the time $z^{unp}_{NeU} = -3$ fm, what Figs. 5 and 6 showed for other times: that as core size is decreased and σ_{NN} increased, the collided matter tends to attain higher nucleon-matter densities and somewhat larger regions of high density. Note the attainment of compression $\rho/\rho_0 \approx 3.0$ for {4πI, 53.1}. Note also that the sensitivity to style is greater for larger σ_{NN}. There is a general foreshortening of the density pattern as σ_{NN} is increased. This is consistent with the idea that large σ_{NN} promotes shocklike behavior.

At the extreme left in Fig. 7 there are two diagrams marked $\sigma_{NN} = 0$. These diagrams extend the range of our sensitivity-to-σ_{NN} results. They are also useful, as will be shown soon, for illustrating some effects from statistical fluctuations and nonzero space resolution. But first we explain how these two $\sigma_{NN} = 0$ diagrams were calculated, and why they differ from each other. Both these $\sigma_{NN} = 0$ diagrams show unperturbed density functions. To calculate each, we simply displaced an ensemble-averaged initial-Ne density function so as to center it at $z = -3$ fm, and then superimposed it on the ensemble-averaged initial-U density function. The upper $\sigma_{NN} = 0$ diagram in Fig. 7 was calculated using the initial density patterns of the {RC, 25.4} ensemble; the lower, {4πI, 15.4}. The two $\sigma_{NN} = 0$ diagrams differ mainly because of statistical fluctuations (and the *degree* of statistical fluctuation may differ for RC and 4πI because of the difference between RC and 4πI restrictions on initial NN separations).

Suppose that there were zero statistical error, perfect space resolution, and no inaccuracies introduced by interpolation. Then each of the two $\sigma_{NN} = 0$ diagrams in Fig. 7 would show an area of $\rho/\rho_0 = 2$ with sharp circular edge, surrounded by an area of $\rho/\rho_0 = 1$ with sharp circular edge. Instead, Fig. 7 shows $\sigma_{NN} = 0$ diagrams with gentle space gradients of ρ, approximately as gentle as those in our $\sigma_{NN} > 0$ diagrams. This reminds us again that, because of nonzero space resolution, our pictures may not convey a very good idea of how sharp the space gradients of $\rho_{\mathcal{E}}$ would be.

The two $\sigma_{NN} = 0$ diagrams in Fig. 7 differ most obviously near small $\tilde{r}$. This jibes with a fact mentioned previously, that the statistical fluctuations tend to be particularly severe near small $\tilde{r}$, where our volume elements are small. There

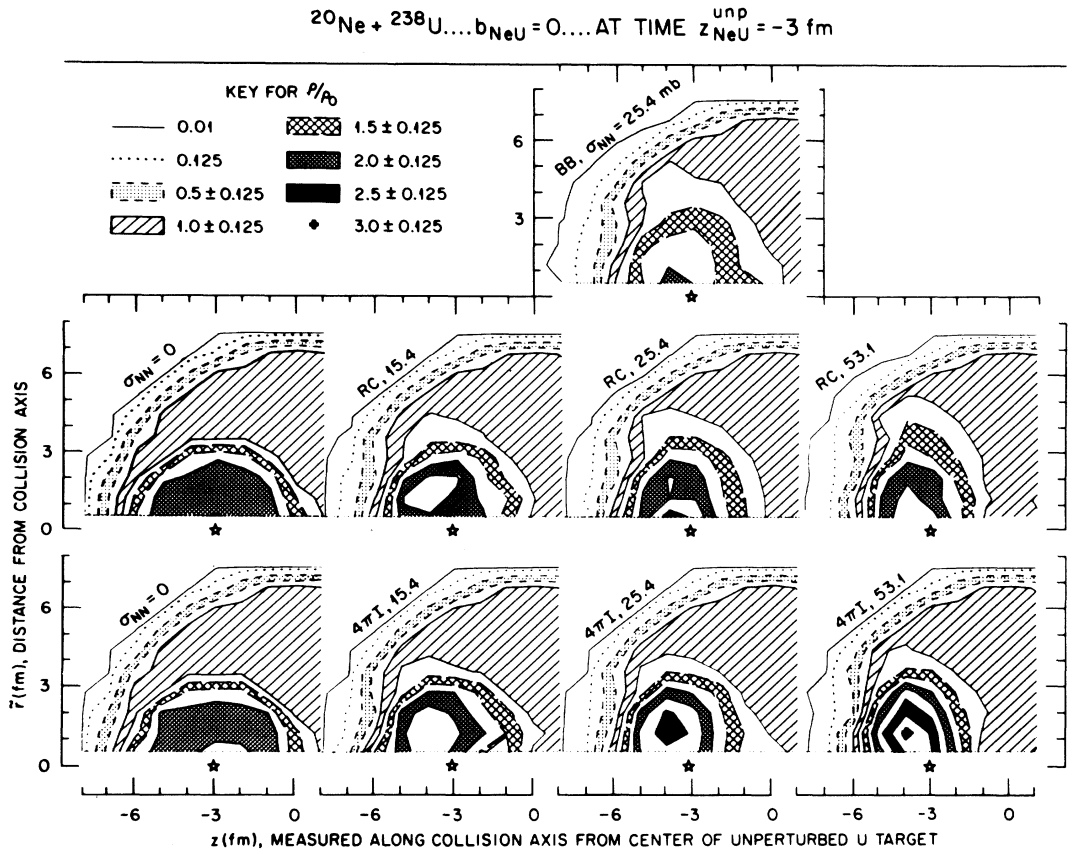

FIG. 7. Contour plots showing sensitivity of nucleon-matter densities to details of the *NN* model. Results are shown for three different *NN* scattering styles (BB, RC, and 4πI) used with various *NN* cross sections (σ_{NN} = 0, 15.4, 25.4, and 53.1 mb). All results are for head-on $^{20}Ne + ^{238}U$ collision at a time corresponding to $z^{unp}_{Neu} = -3$ fm, i.e., when the projectile center would be just 3 fm short of reaching the target center if both nuclei were unperturbed. (It is near this time that most of our models give their maximum ρ/ρ_0.) The bottom right diagram (4πI, 53.1) shows a small region (the innermost black-marked region) where $\rho/\rho_0 = 3.0 \pm 0.125$. For other conventions see the caption to Fig. 4 and the text of Secs. III. A and III. B.

are some other minor problems too, near small $\tilde{r}$. In general, our contour figures are somewhat ambiguous in that *singly bounded* blank areas could imply densities higher or lower than that of their surrounding patterned areas. In perturbed zones during early or middle stages of the collision, such singly bounded blank areas usually correspond to higher density; but in the lower-left $\sigma_{NN} = 0$ diagram of Fig. 7, the central blank area happens to correspond to lower density, $\rho/\rho_0 < 1.875$. We mention one other kind of uncertainty near small $\tilde{r}$: Note that several of the $\sigma_{NN} = 0$ diagrams in Fig. 7 (i.e., several of the diagrams which describe perturbed collided matter) show their highest-density regions away from the smallest-$\tilde{r}$ line, instead of touching the smallest-$\tilde{r}$ line. This kind of result indicates a *torus* of highest density, instead of a central lump of highest density. At present we do not know whether such toroidal patterns should be attributed to statistical fluctuations, or to dynamic causes that would give toroidal patterns even in ρ_δ.

All of the foregoing ρ figures show contour plots. Together they indicate that the highest densities tend to occur near the collision axis and near the time $z^{unp}_{NeU} = -3$ fm. Figure 8 concentrates on these high-density conditions; it shows noncontour plots of ρ/ρ_0 vs z along the collision axis at $z^{unp}_{NeU} = -3$ fm.

Before discussing the main content of Fig. 8, we comment on its format and its statistical-uncertainty features. The noncontour format of Fig. 8 has several advantages. It allows us to show ensemble-averaged functions $\rho(\tilde{r}, z^{unp}_{NeU})$ more directly (without the extra screen of ρ/ρ_0 bins); it allows us to exhibit results for several different ρ functions all very close together (within the same plotting area); and it facilitates the display of *statistical-uncertainty* bars. These bars are helpful for deciding whether the difference between

one ρ function and another is statistically significant or not. In order to increase the statistical significance, we have computed ρ for Fig. 8 using disc-shaped volume elements larger than the on-axis discs used for Figs. 4–7. (If the *same* small on-axis discs were used, then the points in Fig. 8 would vary much more erratically and would have uncertainty bars twice as long.) For quantitative details about the volume elements and uncertainty bars in Fig. 8, see its caption.

In Fig. 8 all of the BB, RC, and $4\pi I$ ρ results have their peaks at $z=-4$ fm. However, we see some clear differences in the peak ρ value, and also in the shape of the peak. The three separate panels (a), (b), and (c) show sensitivity: (a) to NN-scattering style at fixed σ_{NN}, (b) to σ_{NN} at fixed style RC, and (c) to σ_{NN} at fixed style 4πI. For our first look at Fig. 8, we ignore the results for RN (symbols ×) and for $\sigma_{NN}=0$ (dashed line). That is, we consider only the BB, RC, and 4πI results. Then Fig. 8 reassures us that, despite our problems of statistics and space resolution, the following differences are systematic and statisticially significant:

(a) $\rho\{4\pi\text{I},25.4\} > \rho\{\text{RC},25.4\} > \rho\{\text{BB},25.4\}$ in the peak region (i.e., at $z=-5$, -4, -3 fm).

(b) $\rho\{\text{RC},53.1\}$, $\rho\{\text{RC},25.4\}$, and $\rho\{\text{RC},15.4\}$ are successively less steep in their falloff $\partial\rho/\partial z$ beyond the peak at $z=-4$ fm. This is evidenced especially by the results at $z=-1$ fm.

(c) $\rho\{4\pi\text{I},53.1\} > \rho\{4\pi\text{I},25.4\} > \rho\{4\pi\text{I},15.4\}$ in the peak region ($z=-5$, -4, -3 fm). Furthermore, these three ρ functions are successively less steep in their falloff $\partial\rho/\partial z$ beyond the peak at $z=-4$ fm. This is evidenced for example by the results at $z=-1$ fm.

Obviously, our NN scattering style strongly influences the degree of sensitivity to σ_{NN}. For RC there is no significant sensitivity of the maximum ρ/ρ_0 to σ_{NN}, while for 4πI there is considerable sensitivity. The insensitivity for RC suggests that we should not have taken very seriously the Fig. 7 result showing a small black region ($\rho/\rho_0 \approx 2.5$) for $\{\text{RC},25.4\}$. Apparently the volume and the number of counts associated with that small black region are themselves so minor that little statistical significance is implied. (Indeed, this was

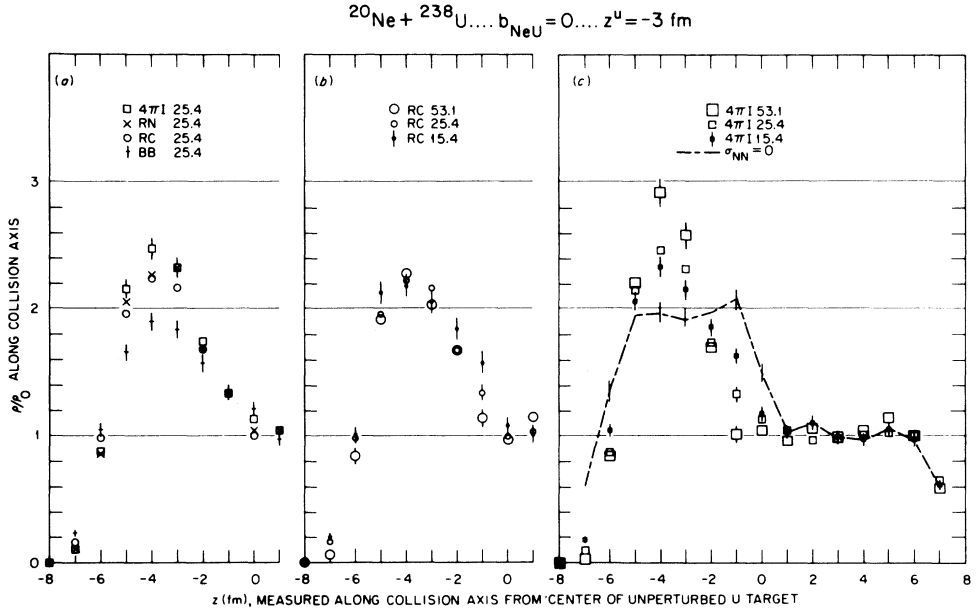

FIG. 8. Comparisons showing how nucleon-matter densities along the collision axis z vary with NN-scattering style (see left panel) and with σ_{NN} in mb (see center and right panels). All results are for head-on ^{20}Ne + ^{238}U collision at a time corresponding to $z^u \equiv z^{\text{ump}}_{\text{NeU}} = -3$ fm [see Eq. (2)]. It is near this time that most of our models give their maximum ρ/ρ_0. The space resolution in this figure is somewhat poorer than in preceding figures, but the statistics are better; for here the plotted densities are averages within disc-shaped volume elements with the usual cylindrical symmetry around the z axis, and with the usual z thickness $\Delta z = 1$ fm, but with outer cylindrical radius $\Delta\tilde{r} = 1.6$ fm instead of 0.8 fm. Thus, each of these on-axis discs has a volume-weighted average $\tilde{r}$ of 1.07 fm instead of 0.53 fm. On some of the plotted points, statistical-uncertainty bars are shown. Each is drawn to represent a fractional uncertainty $\sqrt{\mathfrak{N}}/\mathfrak{N}$ in the value of ρ/ρ_0, where $\mathfrak{N}$ is the total number of nucleons calculated to be in the volume element, accumulated over the pertinent ensemble of collisions. (Exception: when $\mathfrak{N}=0$, the bar is drawn to represent an uncertainty of 1 in $\mathfrak{N}$.) See also the text of Secs. III. A and III. B.

already suggested by the absence of any black region in the {RC, 53.1} diagram of Fig. 7.)

Next we consider the RN results (symbols ×) in Fig. 8. The ρ function from RN (a style which is like RC in some ways but like 4πI in other ways) shows values falling between ρ values from RC and 4πI. However, the results in Fig. 8 show some features which are not systematically sequential for the entire quartet BB, RC, RN, and 4πI. Possibly this nonsequential behavior is due to statistical fluctuations. More likely, it reflects truly nonsequential behavior of the $\rho_{\mathcal{S}}$ functions. Recall that BB, RC, and RN form a sequence decreasing in core size; they are all restricted to in-plane repulsive NN scattering. In contrast, 4πI is alone in using 4π isotropic NN scattering.

Finally we consider the $\sigma_{NN}=0$ result (dashed line) in Fig. 8(c). Note that the rise and fall of the {4πI, 53.1} ρ function resemble, in steepness, the rise and fall of the $\sigma_{NN}=0$ ρ function. Also, recall that these $\sigma_{NN}=0$ results would be infinitely steep if there were zero statistical error, perfect space resolution, and no inaccuracy from interpolation.[53] This suggests that $\rho_{\mathcal{S}}$ for {4πI, 53.1} may also have a very sharply bounded dense region, and more generally, that our space-resolution problems may mask a strong sensitivity of density gradients to σ_{NN}.

C. ρ in off-center collisions

For off-center collisions $\rho_{\mathcal{S}}$ does not have cylindrical symmetry, and therefore we switch to a Cartesian coordinate system for contour displays.

Readers who want to skim this section will find its main points in paragraphs which begin with an italicized word.

Figure 9 shows four successive time stages of $\rho(z, x, t)$ in a central slice around the collision plane (zx) during off-center collision of ^{20}Ne with ^{238}U. The results were calculated for {RC, 25.4} at impact parameter $b_{\mathrm{NeU}}=5$ fm. Before commenting on the space resolution and statistical fluctuations in Fig. 9, we summarize the physical results. For the case of off-center collision, we see some features similar to those seen for $b_{\mathrm{NeU}}=0$. However, for $b_{\mathrm{NeU}}=5$ fm these features are mainly confined to the upper part of the system ($x \gtrsim 0$ in our diagrams). High densities develop soon after geometric contact is made. As the collision proceeds, the struck portions of the target become blasted away. In the upper part of the system, the density decreases gradually with time while a front of low density moves outward and upward into previously unoccupied space. The density in the lower part of the system is somewhat disturbed, but not nearly so much as the upper part. Again (just as in head-on collisions) we fail to see a discrete fireball. However, for $b_{\mathrm{NeU}}=5$ fm we do see a weak "cap" from the projectile. This cap is a low-density remnant of the projectile—a part which has traveled through only a small portion of target matter and has escaped NN scattering.

The contour diagrams in Fig. 9 appear more jagged, fluctuation-plagued, and surface-diffuse than those in our $b_{\mathrm{NeU}}=0$ contour plots, e.g., Fig. 4. The underlying causes are the ensemble sizes (199 in Fig. 9, 300 in Fig. 4) and, more important, the sizes and shapes of the volume elements (see the captions to both figures). Concerning the many blank sections within the diagonally patterned $\rho/\rho_0 \approx 1$ region of Fig. 9, some represent fluctuations upward and some downward. Obviously, many of the minor features observable in Fig. 9 should not be taken seriously. There is particular doubt about features in neighborhoods where crossed contour lines appear, because such crossings indicate local ambiguities in the interpolation evaluation of ρ/ρ_0.[54]

For $b_{\mathrm{NeU}}=5$ fm, we have calculated $^{20}\mathrm{Ne}+^{238}\mathrm{U}$ collisions using styles BB, RC, and 4πI but always with $\sigma_{NN}=25.4$ mb. In general, we find that the peak values of ρ increase as we change from BB to RC to 4πI, and the peak values are similar to those achieved in head-on collision. Figure 10 illustrates these (expected) results by showing the sensitivity of density to NN scattering style at times and places where ρ tends to be large. For more details, see the next two paragraphs.

Figure 10 displays noncontour plots of ρ versus z as calculated from BB, RC, and 4πI for three successive times $z^{\mathrm{up}}_{\mathrm{NeU}} \equiv z^{u}$ during off-center collision, and for several alternative sets of the z-indexed volume elements within which ρ is averaged. Our main reason for showing this variety of times, and this variety of volume-element sets, is that BB, RC, and 4πI differ in the coordinates $(\vec{r}, t)$ at which maximum ρ occurs. However, at each fixed time the main qualitative features are the same for all three volume-element sets.

Because the volume-element sets of Fig. 10 are too complicated to describe in the caption, we describe them here. In all the sets, every volume element is symmetric with respect to the xz plane (as $\rho_{\mathcal{S}}$ is). Furthermore, all the sets have their volume elements concentrated rather near the z-directed line defined by $x=4.52$ fm, $y=0$.[55] A particular volume-element set is labeled by its $\bar{x}$, the volume-averaged x which characterizes every one of its elements. The label $\bar{x}=4.52$ refers to a set of disc-shaped elements; each is cylindrically symmetric about the aforementioned z-directed line ($x=4.52$ fm, $y=0$), and each has

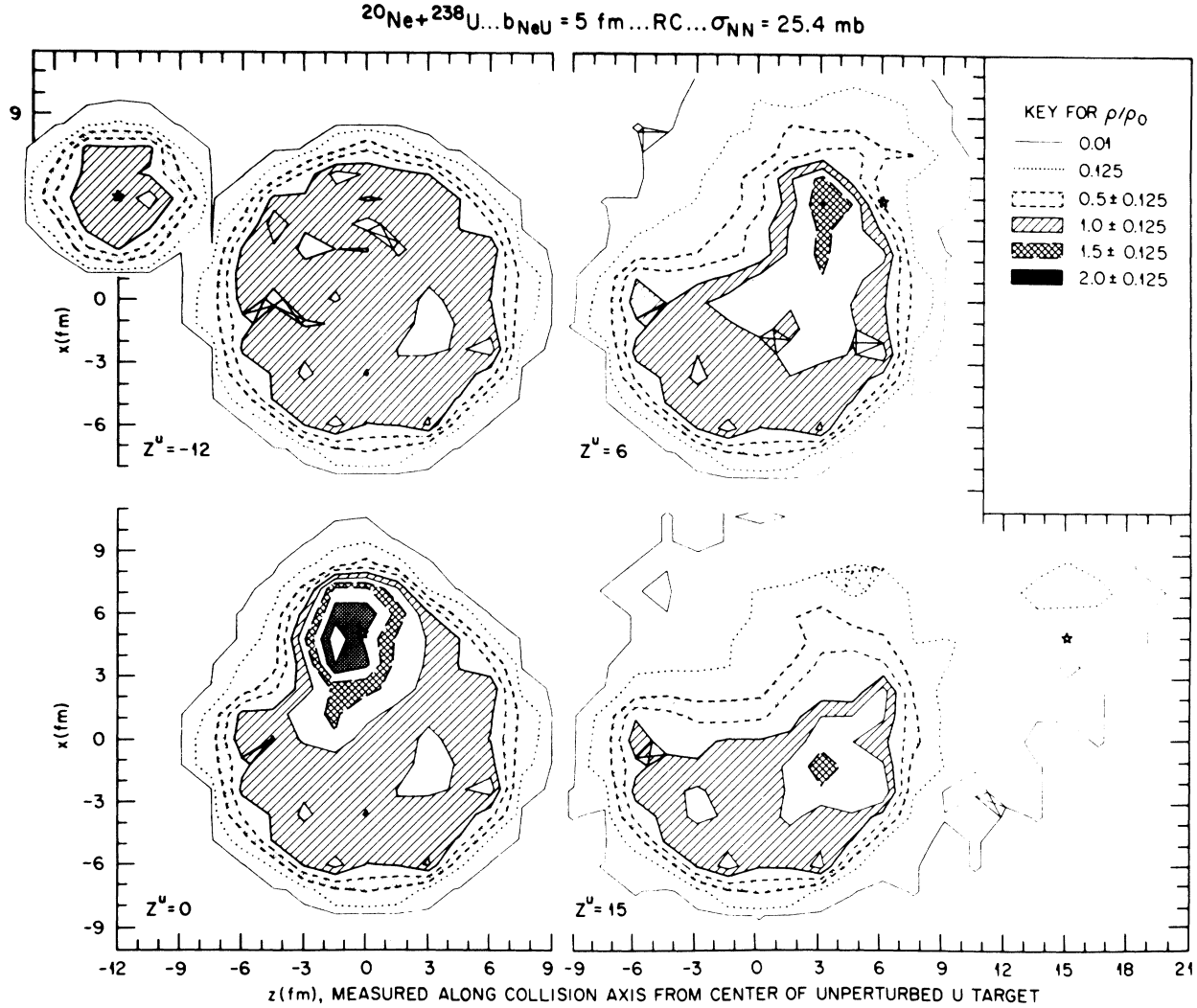

FIG. 9. Contour plots showing time development of the nucleon-matter density near the collision plane xz during ^{20}Ne $+^{238}$U collision at impact parameter $b_{NeU}=5$ fm. Each five-pointed star indicates time by showing where the center of an unperturbed Ne projectile would be. In contrast to the preceding figures, this figure uses Cartesian coordinates. The space resolution is ≥ 1.2 fm because the plotted densities are averages within contiguous volume elements each of dimension $\Delta x=1.2$ fm, $\Delta y=1.5$ fm, $\Delta z=1.5$ fm, all lying within a slab of thickness $\Delta y=1.5$ fm symmetric around the collision plane xz. Thus, each of these elements has a volume-weighted average $|y|$ of 0.38 fm (not 0). For further explanation see the text of Secs. III. A and III. B.

outer radius 1.6 fm with z thickness 1 fm. The label $\bar{x}=5.20$ refers to a special set of half discs, the upper (large x) halves of the $\bar{x}=4.52$ discs; the label $\bar{x}=3.84$ would refer to the lower halves (but that set is not used in Fig. 10). The label $\bar{x}=x_M$ refers to a ρ-dependent set such that at any z, the upper or lower half disc is used, whichever half gives the greater ρ. Thus in the Fig. 10 plots marked $x=\bar{x}_M$, we are comparing the *peak* values of ρ obtained from BB, RC, and 4πI.

D. Differences from fluid-dynamic results

Here we briefly compare our density results with those from some recent fluid-dynamic calculations. We consider the results of Tang and Wong[20] for ^{20}Ne + ^{197}Au at $(E/A)^{\rm LAB}_{\rm BEAM}=250$ MeV—results calculated for head-on collisions assuming two alternative viscosities, small and large. Also, we consider some results of the Frankfurt group[19] for ^{20}Ne + ^{238}U at $(E/A)^{\rm LAB}_{\rm BEAM}=400$ MeV—results cal-

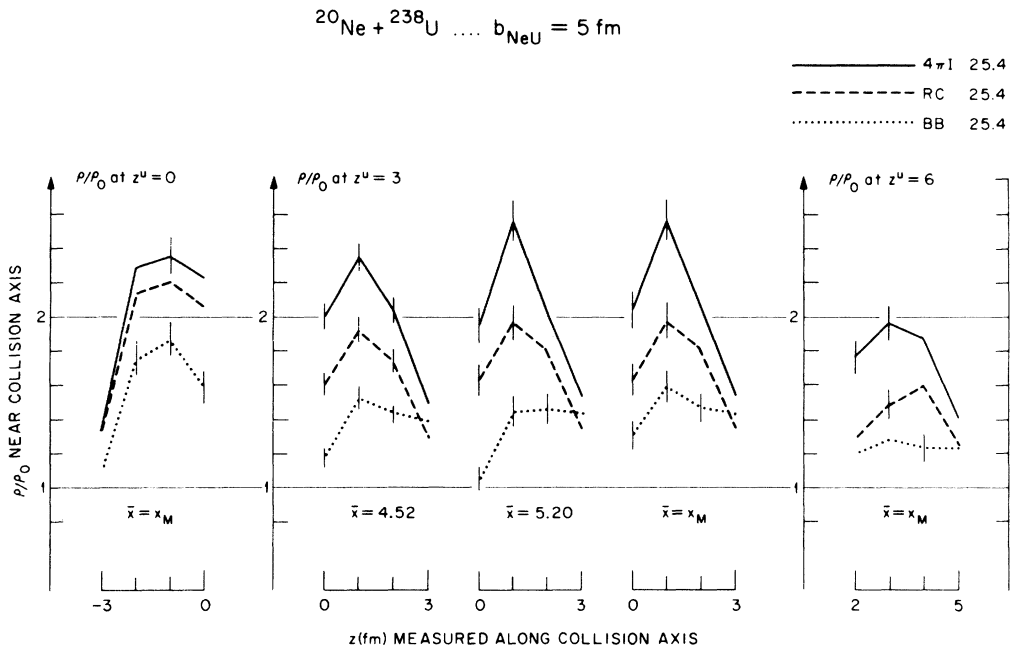

FIG. 10. Comparisons showing how the *NN* scattering style affects peaks in the nucleon-matter density near the collision axis during off-center $^{20}Ne + ^{238}U$ collision ($b_{NeU} = 5$ fm). The comparisons are made among three different *NN*-scattering styles (4πI, RC, and BB) all used with the same *NN* cross section ($\sigma_{NN} = 25.4$ mb). Results are shown for three successive times during collision—times corresponding to $z^u \equiv z^{unp}_{NeU} = 0$, 3, and 6 fm [see Eq. (2)]. For $z^u = 3$ fm three plots are included; they correspond to three alternative sets of the volume elements within which ρ is averaged. For the meanings of the three different labels $\bar{x}$, see the text of Sec. III. C. At some of the plotted points, statistical-uncertainty bars are shown. These are drawn using the same $\sqrt{\mathfrak{N}}/\mathfrak{N}$ prescription mentioned in the caption to Fig. 8. See also the text of Secs. III. A and III. C.

culated for head-on and off-center collisions, assuming small viscosity. All of these fluid-dynamic calculations lead to collided-matter density contours that are more flattened than ours at the struck side of the target. For head-on collisions calculated with small viscosity, the Tang-Wong and also the Frankfurt calculations lead to maximum densities roughly like ours, $\rho/\rho_0 \approx 2$. However, in the Tang-Wong small-viscosity calculations, high compressions are retained for a longer time than in our results. When large viscosity is assumed, the Tang-Wong calculations give maximum ρ/ρ_0 only ≈ 1.3. For head-on collisions the Frankfurt calculations show maximum ρ/ρ_0 at a time that is roughly similar to ours, $z^{unp}_{NeU} \approx -3$ fm. For small and also large viscosity, the Tang-Wong compression maxima occur somewhat later, $z^{unp}_{NeU} \approx 5$ or 6 fm. For off-center collisions with $b_{NeU} \gtrsim 5$ fm, the Frankfurt fluid-dynamic calculations show a collective effect not found in our SIMON results: a projectile fragment which appears to be "bounced off" the target. This fragment, which has $\rho/\rho_0 < 0.4$, is quite clearly separated from the residual target.

IV. FINAL ENERGY-ANGLE DISTRIBUTIONS

In our present simple SIMON models, all particle emission consists of scattered nucleons, each unbound to any other particle. That is why, in Figs. 2 and 3, we compared SIMON 's emission of scattered protons with experimentally determined emission of nucleon charges, the latter summed over discrete protons and larger emitted nuclei. Similarly, SIMON 's emission of scattered nucleons would be compared with experimentally determined emission of nucleon masses, the latter summed over discrete nucleons and larger emitted nuclei.

Figures 11–16 ahead show how some ensemble-averaged yields $d^2n/dEd\Omega$ from $^{20}Ne + ^{238}U$ are affected by b_{NeU}, by *NN* scattering style, and by σ_{NN}. Two kinds of yields are considered. Figures 11–13 deal with proton yields in the laboratory frame, and Figs. 14–16 with nucleon yields in the "equal-speed" frame. Conventions for these figures are explained in subsection A. The physical results are discussed in subsections B and C.

A. Introduction to Figs. 11-16

1. *Basic definitions,* LAB *and* ES *frames,* $\tilde{\text{M}}$eV

We consider first the ensemble-average proton yield per $^{20}\text{Ne}+^{238}\text{U}$ collision:

$$\frac{d^2n_p}{dE_p^{\text{LAB}}d\Omega_p^{\text{LAB}}} \equiv \frac{d^3n_p}{dE_p^{\text{LAB}}d\cos\theta_p^{\text{LAB}}d\phi_p} \text{ averaged over } \phi_p . \tag{4}$$

Each function $d^2n_p/dE_p^{\text{LAB}}d\Omega_p^{\text{LAB}}$ is calculated for fixed impact parameter b_{NeU}, fixed NN scattering style, and fixed σ_{NN}. The symbols n_p, E_p^{LAB}, and Ω_p^{LAB} refer to the number, laboratory kinetic energy, and laboratory velocity angle (with respect to the projectile direction) of scattered protons near the end of a $^{20}\text{Ne}+^{238}\text{U}$ collision. By "near the end" we mean at a time t_{STOP} such that the center of an unperturbed ^{20}Ne projectile would be about three ^{248}U radii past the center of an unperturbed ^{238}U target. (Details about t_{STOP} will be given later.) Our present SIMON code does not label individual nucleons as being in a specific charge state. However, we compute energy-angle distributions for *protons* by taking, for each energy-angle interval, $\frac{10}{20}$ times the number of nucleons originating from ^{20}Ne plus $\frac{92}{238}$ times the number of nucleons originating from ^{238}U. Because ^{20}Ne is so much lighter than ^{238}U, the laboratory frame is close to the c.m. frame of the entire colliding system. Furthermore, it may be considered close to the rest frame of the excited residual target.

Besides the proton yields of Eq. (4), we consider ensemble-averaged nucleon yields defined in a similar way:

$$\frac{d^2n_N}{dE_N^{\text{ES}}d\Omega_N^{\text{ES}}} \equiv \frac{d^3n_N}{dE_N^{\text{ES}}d\cos\theta_N^{\text{ES}}d\phi_N} \text{ averaged over } \phi_N . \tag{5}$$

Here the superscript ES denotes the equal-speed frame, in which the two initial approaching nuclei ^{20}Ne and ^{238}U have equal speeds $\frac{1}{2}v_{\text{NeU}}$. This ES frame is the NN c.m. frame for first scattering, i.e., for the SIMON scattering of a previously unperturbed Ne nucleon with a previously unperturbed U nucleon. The ES frame is a useful one if the energy-angle distributions are dominated either by first-scattering products, or by matter thermalized and emitted shortly after the first contact of the ^{20}Ne and ^{238}U surfaces.

As noted in Sec. II B, simple SIMON's results are completely independent of $(E/A)_{\text{BEAM}}^{\text{LAB}}$ provided that we use time units inversely proportional to v_{NeU}, energy units proportional to $(E/A)_{\text{BEAM}}^{\text{LAB}}$, etc. In Figs. 11–16 we have used such energy units, letting

$$1\ \tilde{\text{M}}\text{eV} = \tfrac{1}{250}(E/A)_{\text{BEAM}}^{\text{LAB}} \tag{6}$$

so that $1\ \tilde{\text{M}}\text{eV} = 1$ MeV when $(E/A)_{\text{BEAM}}^{\text{LAB}} = 250\ \tilde{\text{M}}\text{eV}$.

2. *More about* b_{NeU} *and energy-angle bins*

Because of the ϕ average in Eqs. (4) and (5), each value $d^2n/dEd\Omega$ describes the contribution to $d^2\sigma/dEd\Omega$ from a cylindrically symmetric ring of Ne projectiles all incident at scalar impact parameter b_{NeU}. Such a contribution would be weighted by $2\pi b_{\text{NeU}}db_{\text{NeU}}$ in the integral over impact parameter. The contribution from $b_{\text{NeU}}=0$ has zero weight, but contributions from $b_{\text{NeU}}\approx 5$ fm have major importance for the middle range of E_p^{LAB} and θ_p^{LAB}. This importance is indicated by Table II, which shows $b_{\text{NeU}}d^2n_p^{\text{LAB}}/dE_p^{\text{LAB}}d\Omega_p^{\text{LAB}}$ as a function of b_{NeU} for the particular combination {BB, $\sigma_{NN}=25.4$ mb}.

Next we describe some details affecting the energy-angle resolution and statistical uncertainty in Figs. 11–16. The $(E_p^{\text{LAB}}, \theta_p^{\text{LAB}})$ bins used in Table II are a subset of those used for Figs. 11–13. The complete set consists of contiguous two-dimensional bins. These bins have energy widths $\Delta E = \Delta E_p^{\text{LAB}} = 20\ \tilde{\text{M}}\text{eV}$ (with centers at 10, 30, 50, . . . $\tilde{\text{M}}$eV); and they have angular width either $\Delta\theta_p^{\text{LAB}} = 10°$ (for bins centered at 20°, 30°, . . . , 160°) or $\Delta\theta_p^{\text{LAB}} = 15°$ (for bins centered at 7.5°, 162.5°). For a single bin i, the ϕ-averaged ensemble-averaged yield Y_i is calculated as

$$Y_i \equiv \left(\frac{d^2n}{dEd\Omega}\right)_i = \frac{1}{2\pi}\frac{1}{(\text{ensemble size})}\left[\frac{\mathfrak{N}}{\Delta E\,\Delta(\cos\theta)}\right]_i , \tag{7}$$

where ensemble size is the number of collisions in the ensemble. For proton yields, $\mathfrak{N}$ is the total count of protons in bin i accumulated over all collisions in the ensemble; ΔE and $\Delta(\cos\theta)$ are the appropriate spans of bin i. When labeling proton yields, and also when plotting them, we associate each yield Y_i with its bin-center combination $(E_p^{\text{LAB}}, \theta_p^{\text{LAB}})$. Thus each yield Y_i is plotted as a *point* rather than a histogram level. If the plotted points are connected, they are connected with straight lines.

For nucleon yields in the ES frame, the above description holds after several obvious changes: nucleon replaces proton, N replaces p, ES replaces LAB. But there is also another small set of changes: For nucleons the angular widths are given by $\Delta(\cos\theta_N^{\text{ES}}) = -0.1$, and when plotting we use the angular bin-center coordinates $\cos\theta_N^{\text{ES}} = -0.95, -0.85, \ldots, +0.95$. Furthermore, when plotting nucleon yields vs E_N^{ES} we sometimes consider larger-than-standard bins, formed by combining standard bins so that $\Delta E_N^{\text{ES}} = 20\ \tilde{\text{M}}\text{eV}$ but $|\Delta(\cos\theta_N^{\text{ES}})| > 0.1$.

3. More about t_{STOP}

Our cutoff time t_{STOP} affects $d^2n_p/dE_p^{LAB}d\Omega_p^{LAB}$ strongly for $E_p^{LAB} = 10$ M̃eV, but only weakly for $E_p^{LAB} \geq 30$ M̃eV. This conclusion follows from an investigation we made in which we computed some BB energy-angle yields with and without time cutoff. (In the ensembles without cutoff, each ^{20}Ne $+^{238}$U collision was allowed to proceed until its natural end, that is, until all its 258 nucleons had positions and velocities such that no more NN scatterings could occur.)

By artificially terminating at time t_{STOP}, we are neglecting NN scatterings that occur late during each heavy-ion collision. Such NN scatterings are mainly of the kind that further thermalize a residual excited target consisting of low-energy particles plus not-yet-scattered particles. This explains why the main changes induced by cutoff at t_{STOP} are in the region of nuclear energies close to zero in the laboratory frame. But in that low-energy region, SIMON results tend to be somewhat unreliable anyway, for other reasons: Our simple SIMON code neglects internal kinetic energy in the precollision system, and neglects binding and Coulomb forces throughout.

4. Statistical uncertainties and square-root-scale plotting

We want to see how energy-angle distributions vary with NN scattering style, with σ_{NN}, and with b_{NeU}. For help in deciding whether variations are statistically significant, we include in our figures some statistical-uncertainty bars. To keep all these bars roughly similar in length, we plot most

TABLE II. Relative contribution to $d^2\sigma_p/dE_p^{LAB}d\Omega_p^{LAB}$ from proton yields for different impact parameters b_{NeU} in collisions of ^{20}Ne with ^{238}U. All results were calculated using the NN scattering style BB, with $\sigma_{NN} = 25.4$ mb. Here E_p^{LAB} and θ_p^{LAB} are the medians of energy-angle bins having full widths $\Delta E_p^{LAB} = 20$ M̃eV, $\Delta\theta_p^{LAB} = 10°$. The unit M̃eV is defined in Eq. (6).

E_p^{LAB} (M̃eV)	Impact parameter [a] b_{NeU} (fm)	$b_{NeU}d^2n_p/dE_p^{LAB}d\Omega_p^{LAB}$ (in units of 10^3 fm M̃eV^{-1} sr^{-1}) at various θ_p^{LAB} 30°	60°	90°	120°
50	1.03	49	44	23	5
	3.10	150	111	64	11
	5.17	169	132	56	11
	7.24	110	80	26	3
	9.30	22	10	4	0
70	1.03	28	30	13	1
	3.10	94	83	25	3
	5.17	126	106	20	3
	7.24	58	60	21	0
	9.30	7	15	1	0
90	1.03	19	19	6	0
	3.10	68	58	12	0
	5.17	103	58	10	0
	7.24	51	31	4	0
	9.30	7	63	0	0
110	1.03	16	14	2	0
	3.10	56	40	5	0
	5.17	87	54	4	0
	7.24	53	22	5	0
	9.30	18	0	1	0
150	1.03	7	5	1	0
	3.10	31	15	1	0
	5.17	79	16	1	0
	7.24	55	17	0	0
	9.30	13	0	0	0

[a] The five b_{NeU} values correspond to 0.1, 0.3, 0.5, 0.7, and 0.9 times 1.16 $(20^{1/3}+238^{1/3})$ fm. The ensemble sizes were 350 for $b_{NeU} = 5.17$ fm, and 150 otherwise.

yields on a square-root scale (instead of a linear or log scale). There are more general reasons, too, for choosing a square-root scale. Details follow.

First we explain why all bar lengths are similar, within a given square-root-scale plot. (By similar we mean within a factor of ≈2, which is much more similar than they would be on a linear or log scale.) The uncertainty bar drawn on each yield Y_i is based on a rough estimate of the statistical uncertainty in $\mathfrak{N}$ for bin i; see Eq. (7). Consider first the case of nucleons, for which $\mathfrak{N}$ is a direct count. In this case we take the uncertainty in $\mathfrak{N}$ to be $\pm\sqrt{\mathfrak{N}}$ when $\mathfrak{N}>0$, and 1 when $\mathfrak{N}=0$. It follows that the uncertainty in $\mathfrak{N}^{1/2}$ is about $\pm\frac{1}{2}$ when $\mathfrak{N}>0$, and 1 when $\mathfrak{N}=0$. [To see this, just expand $(\mathfrak{N}\pm\sqrt{\mathfrak{N}})^{1/2}$ in a Taylor series around $\mathfrak{N}^{1/2}$, and realize that since $\mathfrak{N}$ is an integer, $\mathfrak{N}>0$ means $\mathfrak{N}\geq 1$.] For protons the argument is a little more complicated, because for protons $\mathfrak{N}$ is not a direct count but is a weighted sum of two different direct counts. (See the first paragraph of Sec. IV A 1. The complication is easy to handle because $\frac{10}{20}\approx\frac{92}{238}$.) For protons as well as nucleons, we conclude that the magnitude of the uncertainty in $\mathfrak{N}^{1/2}$ is approximately a constant when $\mathfrak{N}>0$, and is twice that constant when $\mathfrak{N}=0$. Then to use this $\mathfrak{N}^{1/2}$ information for estimating the uncertainty in $Y_i^{1/2}$, we invoke Eq. (7), taking the square root of both sides. We conclude that the magnitude of the uncertainty in $Y_i^{1/2}$ is roughly independent of $\mathfrak{N}$ but varies as $\{(\text{ensemble size})[\Delta E\,\Delta(\cos\theta)]_i\}^{-1/2}$. The latter variation is mild, within any one of our square-root-scale figures, for the following reasons. Our widths ΔE are constant at 20 MeV, our standard widths $\Delta(\cos\theta_N^{\rm ES})$ are constant at 0.1, our widths $\Delta(\cos\theta_p^{\rm LAB})$ vary from least to greatest by a factor of 5.1, and our ensemble sizes range only from 199 to 300 (see Table I). In short, within any one of our square-root-scale figures, the magnitude of the statistical uncertainty in $Y_i^{1/2}$—*a magnitude that is represented by the length of the associated uncertainty bar*—varies only mildly. Since all statistical-uncertainty bars would be roughly equal in length, we do not show very many explicitly; a few samples are enough.

More generally, by plotting most yields on a square-root scale (instead of a linear or log scale), we are distributing the proper proportions of plot-space to yield-curve sections of differing magnitudes. Here "proper" implies that if two bumps in a yield curve have about the same height, then both bumps have about the same statistical significance (even if one of these bumps occurs in a large-yield section of the curve while the other occurs in a small-yield section). It is just this kind of equity which is assured by choosing a scale that makes all statistical-uncertainty bars similar in length. To state the case another way: When we draw a graph showing curves of yield vs energy or angle, we want to devote most of the plot area to larger-yield portions of the curves, where functional variations are statistically more significant. Conversely, we want to avoid devoting large amounts of space to details of the statistical fluctuations that plague small-yield portions of our curves. On a log scale these statistical fluctuations in small-yield curve-portions loom large, taking up proportionately more space than they are worth. A linear scale causes problems of the opposite kind: it inhibits examination of all detail except in curve sections showing our largest few yield points. A square-root scale is the right compromise. A related advantage is this: A square-root scale, unlike a log scale, allows us to plot, explicitly, yields which are calculated to be zero (no counts in the bin).

5. *Choice of energy-angle ranges in laboratory-frame figures*

In each of Figs. 11–12 we plot $d^2n_p/dE_p^{\rm LAB}d\Omega_p^{\rm LAB}$ vs $\theta_p^{\rm LAB}$ for two energy groups, $E_p^{\rm LAB}\approx 70$ and 150 MeV. When $(E/A)_{\rm BEAM}^{\rm LAB}\gtrsim 250$ MeV (so that 70 MeV $\gtrsim 70$ MeV), both 70 and 150 MeV are away from the the small-energy region that may be seriously affected because our SIMON models neglect NN binding forces and neglect internal kinetic energy of the initial nuclei. Furthermore, as Figs. 11–13 indicate directly, our displays avoid those regions at large angles and/or high energies where small calculated yields lead to very serious statistical uncertainty. Finally, by comparison with Figs. 2 and 3 it may be seen that, for the most part, Figs. 11–13 avoid those regions at large angles toward high energies where SIMON's proton-emission results (integrated over impact parameter) disagree by orders of magnitude with experimentally determined results.

B. Laboratory-frame results for proton emission

Here, and also in the next subsection, when we assess the sensitivity of yields to style, to σ_{NN}, and to $b_{\rm NeU}$ we generally have in mind a comparison with statistical uncertainty. Therefore a *big* change in yield is one that looks big on our square-root-scale plots, where the ordinate increases linearly with the square root of yield. Readers who want to skim this subsection will find its main points in paragraphs which begin with an italicized word.

Figure 11 shows head-on-collision results. The left panel displays sensitivities to scattering style

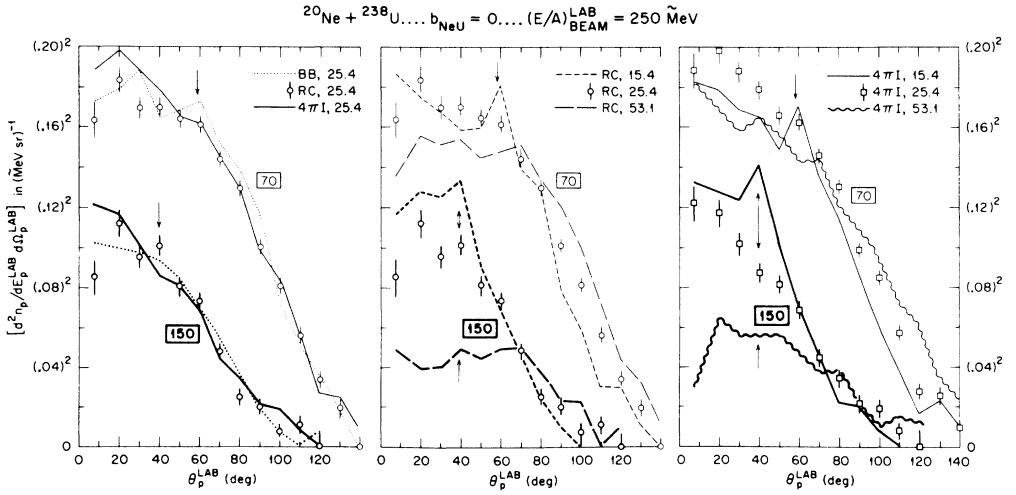

FIG. 11. Double-differential scattered-proton yields in the laboratory frame, per head-on $^{20}Ne + ^{238}U$ collision, as calculated for two different proton energy groups: $E_p^{LAB} \approx 70$ and 150 MeV. The left panel shows sensitivity to NN scattering style, while the center and right panels show sensitivity to σ_{NN} in mb. All energies are in MeV, a unit which equals $\frac{1}{250}(E/A)^{LAB}_{BEAM}$. The arrows indicate first-scattering combinations $\{E_p^{LAB}, \theta_p^{LAB}\}$—i.e., combinations which could result from the SIMON scattering of a previously unscattered Ne nucleon with a previously unscattered U nucleon. Statistical-uncertainty bars are not shown explicitly for all the curves, but for a given θ_p^{LAB} their lengths would be $\lesssim 1.2$ times the length of the exhibited bar. For further explanation see the text of Secs. IV. A and IV. B.

(with σ_{NN} fixed at 25.4 mb), while the central and right panels display sensitivities to σ_{NN} (for styles RC and 4πI, respectively). A first look shows this: Within the exhibited range of NN scattering styles and σ_{NN}, the function $d^2n_p/dE_p^{LAB}\,d\Omega_p^{LAB}$ shows much more sensitivity to σ_{NN} than to style. There is especially striking sensitivity to σ_{NN} when $\theta_p^{LAB} < 60°$ and $E_p^{LAB} \approx 150$ MeV (as opposed to 70 MeV).

In the same energy-angle regions where Fig. 11 shows greatest sensitivity to σ_{NN}, larger σ_{NN} produces smaller yields.

The enhanced multiple scattering caused by larger σ_{NN} is shifting the scattered-proton yield to other energies and other angles. Multiple scattering promotes thermalization in the overall c.m. system, which is close to the laboratory system. Therefore we expect that large σ_{NN} will promote shifts toward large laboratory angles and also toward small laboratory energies (yet smaller than 70 MeV). These expectations are consistent with the results shown in Fig. 11 (and also Fig. 13 ahead).

Closer examination of Fig. 11 shows that, for both 70 and 150 MeV, the three smallest-angle points ($\theta_p^{LAB} = 7.5°, 20°, 30°$) involve some fluctuating angular behavior and quite noticeable sensitivity to scattering style as well as to σ_{NN}. These fluctuations with angle change (indeed *fluctuate*) with energy.[56] The fluctuations seem to have statistical significance, but at present we do not really understand them. We speculate that they are associated with low-multiple scattering (e.g., with doubly-scattered protons) and with the geometry of the target and projectile surfaces. We suspect that these fluctuations would be suppressed by assuming diffuse surfaces for the precollision nuclei.

In Fig. 11 there appear several vertical arrows. These indicate first-scattering combinations $\{E_p^{LAB}, \theta_p^{LAB}\}$, i.e., combinations which could result from the SIMON scattering of a previously unscattered Ne nucleon with a previously unscattered U nucleon. For each curve of Fig. 11, all first-scattering contributions would fall within a single energy-angle bin, i.e., would contribute to a *single* point. (See Sec. II B and Appendix A for discussion of first-scattering combinations $\{E, \theta\}$ and their effective widths—these widths being dependent on the widths of our energy-angle bins.) Since large σ_{NN} encourages multiple scattering, we expect that as σ_{NN} increases, the relative importance importance of first-scattering contributions will decrease. Figure 11 confirms this. Here are some details: For $\sigma_{NN} = 15.4$ mb, Fig. 11 includes four curves, and every one of these four has a peak clearly implying a first-scattering contribution. For $\sigma_{NN} = 25.4$ mb, Fig. 11 includes six different curves, and together these show two fairly clear first-scattering peaks, plus three bulges which are possibly associated with first scattering. For $\sigma_{NN} = 53.1$ mb, Fig. 11 includes four curves, but only one of these shows a peak in the bin to which first scatterings would contribute. There seems little tendency for first-scattering

contributions to be sensitive to NN scattering style. If there is any such tendency, it is this: At large σ_{NN}, style 4πI suppresses first-scattering contributions more than RC does.

We can also use Fig. 11 to look for some second-order effects concerning sensitivity. One question is: How does σ_{NN} affect sensitivity to style? We have already noted that at $\sigma_{NN}=25.4$ mb, the energy-angle yield of protons is not very sensitive to style. At smaller σ_{NN} we would expect even less sensitivity but at larger σ_{NN} greater sensitivity; we expect this because smaller σ_{NN} means longer mean free path and presumably less dependence on the nonasymptotic details of any particular NN scattering. Our expectation is confirmed, but only mildly, by comparisons across panels in Fig. 11. (This particular second-order effect seemed stronger for particle density ρ. Looking back at Fig. 7 we see that for $\sigma_{NN}=15.4$ mb, ρ looks rather insensitive to the change from RC to 4πI; but for $\sigma_{NN}=53.1$ mb, ρ looks quite sensitive to this change.) Another question about second-order sensitivity is: How does scattering style affect sensitivity to σ_{NN}? Figure 11 indicates that the sensitivity of yield to σ_{NN} is very similar for RC and 4πI, and if not exactly the same, then a little greater for RC than for 4πI. (This particular second-order effect differs from that observed for particle density ρ. Looking back at Fig. 7, we see that ρ looks rather insensitive to σ_{NN} for RC, but is clearly sensitive to σ_{NN} for 4πI.)

Next we extend our consideration to off-center collisions. For $b_{NeU}=5$ fm, calculations were made with several different NN scattering styles but only our standard cross section, $\sigma_{NN}=25.4$ mb. These calculations showed the energy-angle yield to be only mildly sensitive to style—about as sensitive as was shown for $b_{NeU}=0$ in Fig. 11. Therefore we have limited our displays of off-center results to style RC.

Figure 12 shows off-center RC results (dashed lines), compared with head-on RC results (circle-points), for two emitted-proton energy groups, $E_p^{LAB}\approx 70$ and 150 MeV. At 70 MeV for all angles, the yields from $b_{NeU}=0$ (open circles) exceed those from $b_{NeU}=5$ fm (dashed line); but in the energy-angle region $\{150$ MeV, $\theta_p^{LAB}\leq 50°\}$ the opposite ordering is seen. Our explanation is as follows. The total number of scattered particles, and the relative importance of multiple scatterings, are both greater for $b_{NeU}=0$ than for $b_{NeU}=5$ fm[57] because $b_{NeU}=0$ offers more opportunity for NN scattering. Thus the *overall* yield of scattered protons is greater for $b_{NeU}=0$ than for $b_{NeU}=5$ fm, but *in a limited energy-angle region* the double-differential yield may be smaller for $b_{NeU}=0$ because stronger multiple scattering has the effect

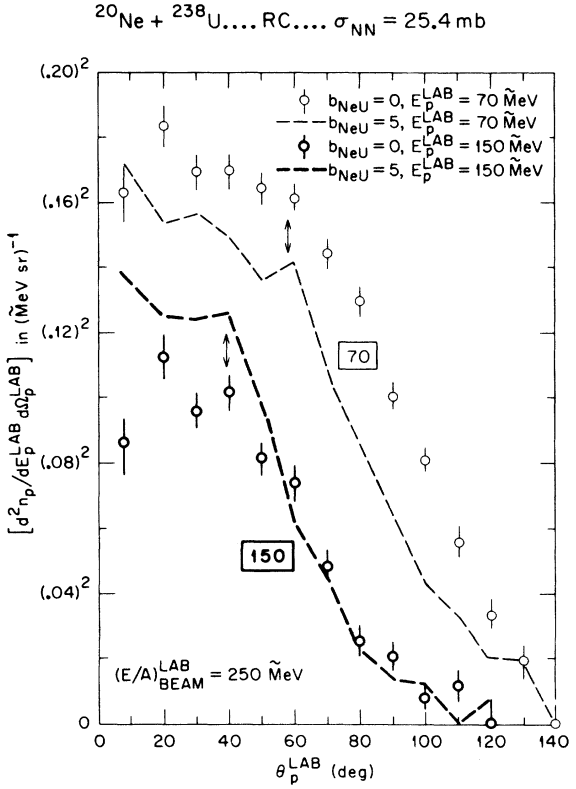

FIG. 12. Double-differential scattered-proton yields in the laboratory frame, per ^{20}Ne + ^{238}U collision, at head-on impact ($b_{NeU}=0$) and at off-center impact ($b_{NeU}=5$ fm). Results are shown for two different proton energy groups: $E_p^{LAB}\approx 70$ and 150 MeV. All results here were calculated using the NN scattering style RC with $\sigma_{NN}=25.4$ mb. For explanations of the energy units MeV, the arrows, and the statistical-uncertainty bars, see the caption to Fig. 11 and the text of Secs. IV. A and IV. B.

of shifting finally-emitted protons to other energy-angle regions. In particular, the $b_{NeU}=0$ yields have a greater tendency to resemble a laboratory-thermalized contribution. At $E_p^{LAB}\approx 150$ MeV (heavy curves in Fig. 12) the shifting effect is strong enough so that the yields from $b_{NeU}=0$ (circle points) fall below the yields from $b_{NeU}=5$ fm (dashed curve). In contrast, energies near 70 MeV are important enough, in a distribution that is approximately laboratory-thermalized, so that the multiple-scattering transfer away from 70 MeV is too mild to destroy the feature of greater emission for $b_{NeU}=0$ than for $b_{NeU}=5$ fm.

Obviously there is a close resemblance between our discussions of the sensitivity to σ_{NN} as shown in Fig. 11, and the sensitivity to b_{NeU} as shown in Fig. 12. Increasing σ_{NN} and decreasing b_{NeU} each produce both more scattered particles and also more scattering per particle.[57] Thus, increasing

σ_{NN} and decreasing b_{NeU} each lead to the same sort of competition—competition between an increased *overall* yield, and a decreased *proportion-of-yield* within a limited energy-angle region. Of course the details of the ensemble-average multiple-scattering history (e.g., *which* first-scattered nucleons get rescattered before emerging) are determined by several interacting influences: σ_{NN}, the macroscopic geometry of the nuclear collision, and the microscopic geometry of the NN scattering style.

Figure 13 is another display of $d^2n_p^{LAB}/dE_p^{LAB}d\Omega_p^{LAB}$, but it shows this yield plotted against E_p^{LAB} instead of θ_p^{LAB}.

Before analyzing this figure in detail, we describe its main purposes and its special features. Figure 13 illustrates the sensitivity to σ_{NN} for b_{NeU} fixed at 0. Also, Fig. 13 compares yields from $b_{NeU}=0$ and $b_{NeU}=5$ fm for $b_{NeU}=5$ the sensitivity of yield to style is about as mild as was shown for $b_{NeU}=0$ in Fig. 11; therefore we have limited Fig. 13 to RC results. Note the change in vertical scale at 0.04 $(\tilde{\text{M}}\text{eV sr})^{-1}$. In order to retain the advantages of a square-root scale for most of the yields plotted, and yet include the large yields which occur at low E_p^{LAB}, we have used a square-root scale in the lower section and a log scale in the upper section.

To begin our detailed analysis of Fig. 13, we concentrate on the $b_{NeU}=0$ results (drawn with thick curves and points) and ignore the $b_{NeU}=5$ fm results (lightly drawn). We see that for the lowest energies ($E_p^{LAB} \lesssim 60$ $\tilde{\text{M}}$eV), and for all energies at large angles ($\theta_p^{LAB} \approx 110°$), the yields from $b_{NeU}=0$ vary directly with σ_{NN}; i.e., larger σ_{NN} leads to larger yield. This behavior is consistent with our previously mentioned notions that large σ_{NN} gives more scattering, that more scattering implies more multiple scattering, that multiple scattering tends to concentrate yield in a thermalized contribution, and that thermalized contributions dominate at low energies and at large angles. In the energy-angle region $\{E_p^{LAB} \gtrsim 60$ $\tilde{\text{M}}$eV, $\theta_p^{LAB} \lesssim 40°\}$, the yields from $b_{NeU}=0$ vary inversely with σ_{NN}, and we conclude that in this energy-angle region, nonthermal contribu-

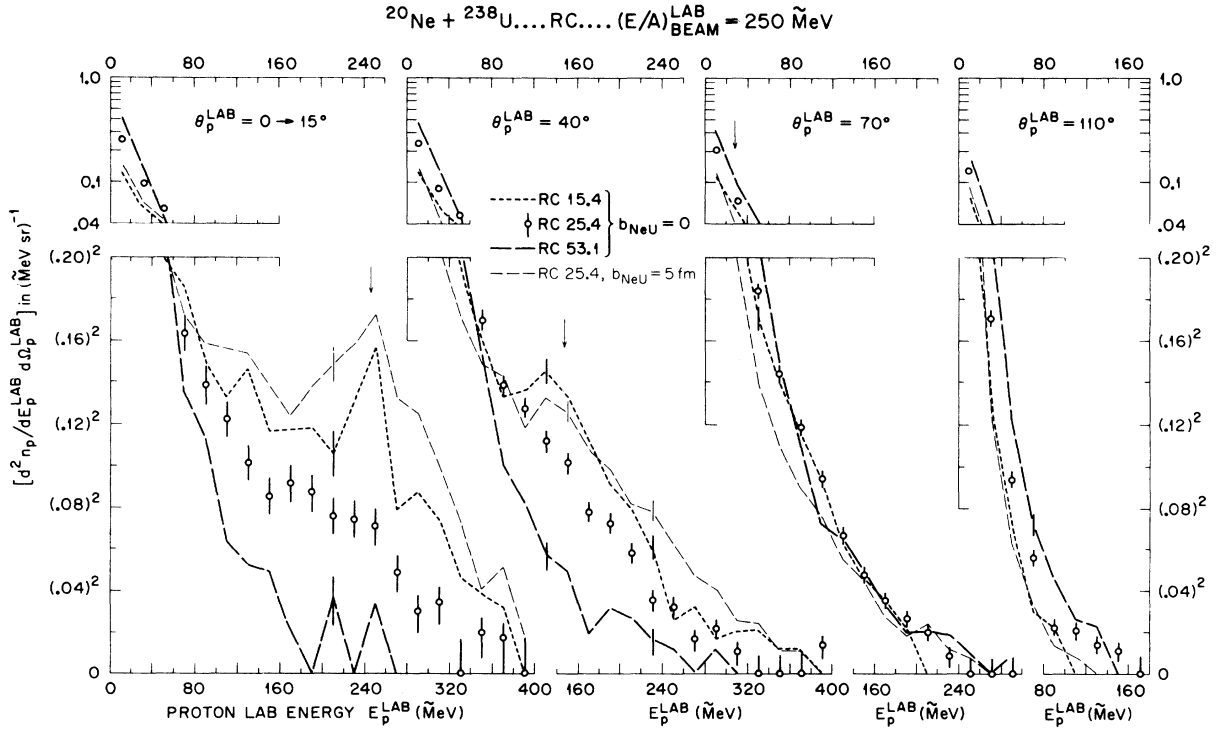

FIG. 13. Double-differential scattered-proton yields in the laboratory frame, per ^{20}Ne + ^{238}U collision, as calculated for four different angular groups of protons. The key that appears in the 40° panel is applicable to all four panels. Thus within each panel, the three heavy curves show the sensitivity to σ_{NN} for head-on collisions ($b_{NeU}=0$), while the lightly drawn curve shows off-center results ($b_{NeU}=5$ fm) calculated with our standard $\sigma_{NN}=25.4$ mb. Note that in the lower section of this figure we use a square-root scale for yield, and in the upper section a log scale. In the 0→15° panel the first-scattering arrow is drawn for $\theta_p^{LAB}=7.5°$. For further explanation of the arrows, the energy units, and the statistical-uncertainty bars, see the caption to Fig. 11 and the text of Secs. IV. A and IV. B.

tions are important. At the intermediate value $\theta_p^{\rm LAB} = 70°$, the yields from $b_{\rm NeU} = 0$ are relatively insensitive to σ_{NN}. In the regions near the first-scattering arrows of Fig. 13, the yields from $\{b_{\rm NeU} = 0,\ \sigma_{NN} = 15.4$ mb$\}$ show clear peaks when $\theta_p^{\rm LAB} \leq 40°$. For the higher σ_{NN} values, the first-scattering contributions must have considerably less relative importance, because they do not give obvious peaks.

Still focusing on $b_{\rm NeU} = 0$ results, we now consider more carefully some details about the widths of the $b_{\rm NeU} = 0$ first-scattering peaks. The formula for first-scattering energy-angle combinations is obtained from Eq. (1) by interpreting $(E_{\rm out}^{\rm LAB}, \theta_{\rm out}^{\rm LAB})$ as $(E_p^{\rm LAB}, \theta_p^{\rm LAB})$. The centers and the widths of our proton energy-angle bins are specified just before Eq. (7), and the consequent widths of SIMON first-scattering contributions are discussed in Appendix A. Using all this information, one can calculate that in Fig. 13, first-scattering contributions should affect the yield results at two energies in the 0–15° panel (230 and 250 MeV) and at three energies in the 40° panel (130, 150, and 170 MeV). In the 0–15° panel, the only clear first-scattering peak for $b_{\rm NeU} = 0$ is for $\sigma_{NN} = 15.4$ mb (short dashes), and it shows the expected width. In the 40° panel, the only clear first-scattering peak for $b_{\rm NeU} = 0$ is again for $\sigma_{NN} = 15.4$ mb (short dashes); but close examination shows that this peak is shifted a little to lower energies—or perhaps it is simply broadened; in any case it starts at 110 MeV rather than 130 MeV. One might think this shift, or slight broadening, is due simply to statistical uncertainty. However, looking back at the first-scattering peaks in Figs. 11–12 (peaks that should be only one bin wide), we see some hints of broadening on the low-$\theta_p^{\rm LAB}$ side. That is, for several of these single-bin peaks, the neighboring lower-energy bin has a yield which is higher than one would expect by extrapolating from the slope at yet lower energies. We shall return very soon to this matter of shifted or broadened $b_{\rm NeU} = 0$ peaks, but before that, we consider the results shown in Fig. 13 for $b_{\rm NeU} = 5$ fm.

In Fig. 13 the results for $\{b_{\rm NeU} = 5$ fm, $\sigma_{NN} = 25.4$ mb$\}$ are shown as lightly drawn dashed curves. In general, they lie rather close to the curves for $\{b_{\rm NeU} = 0,\ \sigma_{NN} = 15.4$ mb$\}$, which are shown as thick short-dashed curves. This closeness is consistent with our previous remark that the effect of increasing $b_{\rm NeU}$ is similar to the effect of reducing σ_{NN}. The most noticeable difference between the results for $\{b_{\rm NeU} = 0, 15.4$ mb$\}$ and $\{b_{\rm NeU} = 5$ fm, 25.4 mb$\}$ is in the 0–15° panel of Fig. 13. Consider the very broad peak given by $b_{\rm NeU} = 5$ fm near the first-scattering arrow. This peak covers many more $E_p^{\rm LAB}$ points than the two points (at 230 and 250 MeV) which can be associated with the width of our energy-angle bins. This broad peak is not just a statistical fluctuation, for we find the same broadness in our other yield results for $b_{\rm NeU} = 5$ fm, e.g., in results from BB and 4πI (not illustrated). Our explanation is only speculative. We speculate that double scattering (as opposed to single or highly-multiple scattering), coupled with geometric effects, leads to broad peaks of this kind. There is probably a relation between the hints of broadness that we see in the $b_{\rm NeU} = 0$ peaks of Figs. 11–13, and the broadness of the peak for $b_{\rm NeU} = 5$ fm seen in the first panel of Fig. 13. Of course, in real heavy-ion collisions, initial Fermi motion (which our SIMON models neglect) would also broaden such peaks.

All of the preceding results and discussion support these ideas: *Several different kinds of contributions make up the emitted-proton energy-angle yield, and furthermore, the proportions of these contributions vary with the energy-angle region and* σ_{NN}. As Fig. 11 indicates, first scatterings do not dominate the emitted-proton yield, nor is the thermalized contribution all-important. A simple fireball model[11] cannot be appropriate for all of the conditions described in Fig. 11. (Suppose that a simple fireball model *were* appropriate for all the σ_{NN} choices, scattering styles, and energy-angle regions of Fig. 11. Then the computed yields would be insensitive to σ_{NN} and to scattering style for all of the energy-angle regions shown and there would be no first-scattering peaks either.) We find that the sensitivity of yield to σ_{NN} varies with energy-angle region, and to a lesser extent this sensitivity varies with σ_{NN} also. The variation of these sensitivities, as well as the variation of the energy-angle yield itself, indicates a variation in the proportions of different sources of contributions to the yield.

The complexities of the mixture of thermalized and nonthermalized contributions—in particular, the sensitivities of this mixture to energy, angle, σ_{NN}, and $b_{\rm NeU}$—argue for using detailed cross sections $d^2\sigma_{\nu N}/dE_{NN}d\Omega_{NN}$ and a fully three-dimensional cascade code, if one wants to calculate the detailed consequences of assuming that only ordinary physical phenomena occur during high-energy heavy-ion collisions. (Of course, there remains the problem of whether free NN cross sections are realistic effective ones, when combined with the other features of a particular intranuclear cascade code.)

C. ES-frame results for nucleon emission

In the equal-speed (ES) frame, the two initial approaching nuclei ^{20}Ne and ^{238}U have equal speeds

$\frac{1}{2}v_{NeU}$. As remarked earlier, this frame would be especially convenient for energy-angle distributions dominated by first-scattering contributions. Suppose that all emitted nucleons were first-scattered nucleons. Then all would have $E_N^{ES} = \frac{1}{4}(E/A)_{BEAM}^{LAB} = 62.5$ M̃eV, and consequently all would be in our energy group characterized by the median $E_N^{ES} = 70$ M̃eV (since this group spans 60 to 80 M̃eV). The angular distribution would be isotropic. However, for our models this supposition of "first scattering only" is far from the truth. Figures 14–16 show that $d^2n/dE_N^{ES}d\Omega_N^{ES}$ is far from being confined to the energy group $E_N^{ES} \approx 70$ M̃eV, and is far from being isotropic either in this energy group or others.

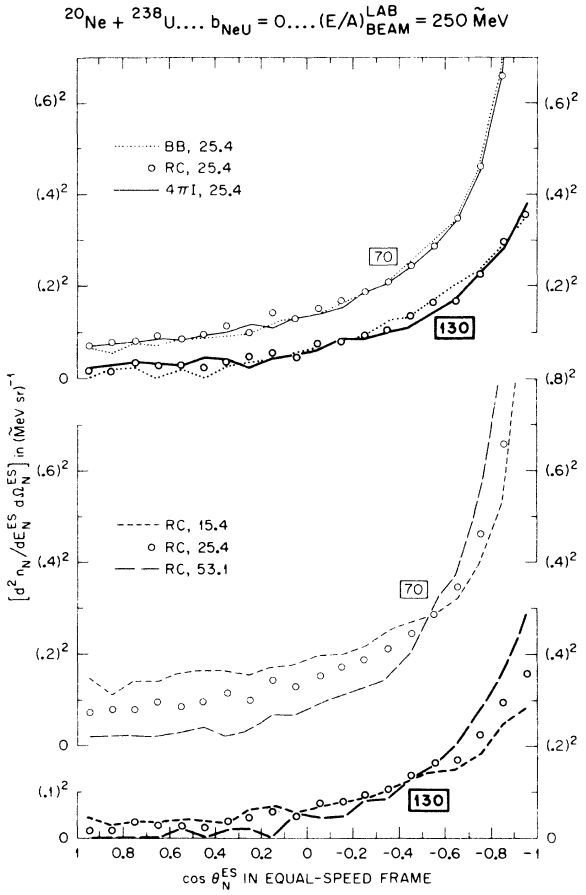

FIG. 14. Double-differential scattered-nucleon yields in the equal-speed frame, per head-on $^{20}Ne + ^{238}U$ collision, as calculated for two different nucleon energy groups: $E_N^{ES} \approx 70$ and 130 M̃eV. The uppermost section of this figure shows sensitivity to *NN* scattering style, while the lower two sections show sensitivity to σ_{NN} in mb. All energies are in M̃eV, a unit which equals $\frac{1}{250}(E/A)_{BEAM}^{LAB}$. The 70-M̃eV group includes nucleons ranging from 60 to 80 M̃eV; therefore it includes all nucleons with $E_N^{ES} = 62.5$ M̃eV, and so it includes all nucleons which would result from the SIMON scattering of a previously unscattered Ne nucleon with a previously unscattered U nucleon. (This last-mentioned contribution would be isotropic.) The circle points are all drawn with diameter about 0.9 times the length that their statistical-uncertainty bars would have. The bar lengths for other curves would be $\lesssim 1.3$ times the circle diameters. For further explanation see the text of Secs. IV. A and IV. C.

Figure 14 shows head-on-collision results. In general, Fig. 14 contrasts insensitivity to *NN* scattering style (see uppermost section) with positive sensitivity to σ_{NN} (lower two panels). For details about statistical uncertainties, see the caption. In both of the energy groups considered in this figure, $E_N^{ES} \approx 70$ and 130 M̃eV, the nucleons emitted near $\cos\theta^{ES} = -1$ have very small energies in the LAB system, i.e., very small energies in the rest frame of the residual target. This implies that the large backward peaks in this figure can be associated with a thermalized contribution. It is away from this thermalized region (i.e., it is in the region $1 \leq \cos\theta_N^{ES} \lesssim -0.5$) that we find yield varying inversely with σ_{NN}. Such behavior is consistent with notions already mentioned several times previously, in connection with Figs. 11–13: Increasing σ_{NN} increases overall scattering, particularly promotes multiple scattering, thereby increases thermalization, and thereby shifts emitted-particle yield away from energy-angle regions less favored by thermalized contributions and toward energy-angle regions more strongly favored by highly thermalized contribu-

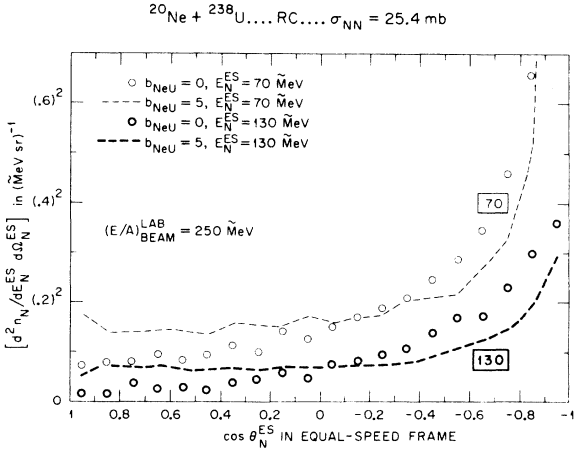

FIG. 15. Double-differential scattered-nucleon yields in the equal-speed frame, per $^{20}Ne + ^{238}U$ collision, at head-on impact ($b_{NeU} = 0$) and at off-center impact ($b_{NeU} = 5$ fm). Results are shown for two different nucleon energy groups: $E_N^{ES} \approx 70$ and 130 M̃eV. All results here were calculated using the *NN* scattering style RC with $\sigma_{NN} = 25.4$ mb. For comments about the energy units M̃eV, the choice of 70 M̃eV, and the statistical uncertainties, see the caption to Fig. 14 and the text of Secs. IV. A and IV. C.

tions.

Figure 15 includes results for the same two energy groups, $E_N^{ES} \approx 70$ and 130 MeV; but it includes results from $b_{NeU} = 5$ fm as well as $b_{NeU} = 0$. Since there is little sensitivity to NN scattering style, we have restricted this figure to style RC. Again we see large thermal peaks toward $\cos\theta_N^{ES} = -1$. Comparison with Fig. 14 indicates that increasing b_{NeU} has the same qualitative effect as decreasing σ_{NN}. As noted earlier, this is understandable because increasing b_{NeU} and decreasing σ_{NN} both decrease the opportunity for NN scattering.

Figure 16 shows head-on-collision results for

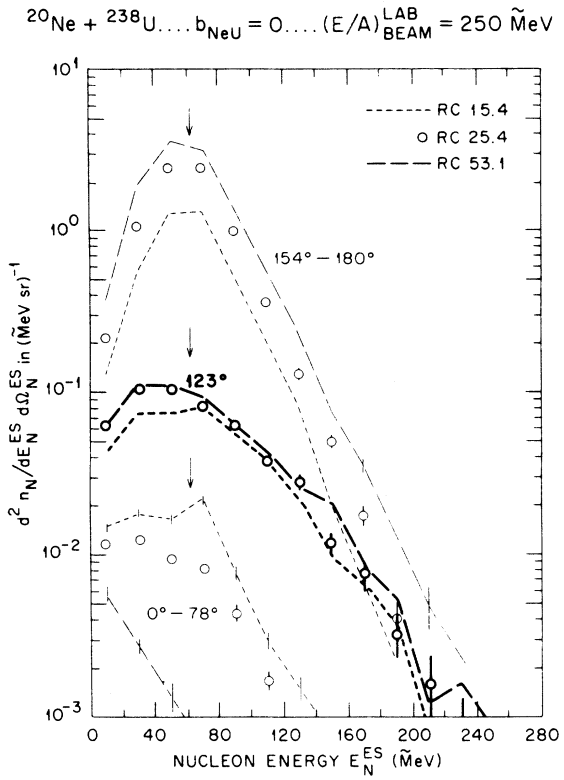

FIG. 16. Double-differential scattered-nucleon yields in the equal-speed frame, per head-on $^{20}Ne + ^{238}U$ collision, as calculated for three different angular groups of nucleons. The label 154°–180° implies $\cos\theta_N^{ES}$ ranging from −0.9 to −1.0; the label 123° implies $\cos\theta_N^{ES}$ from −0.5 to −0.6; the label 0°–78° implies $\cos\theta_N^{ES}$ from 1.0 to 0.2. Each arrow indicates $E_N^{ES} = 62.5$ MeV, which is the energy of any nucleon emerging from the SIMON scattering of a previously unscattered Ne nucleon with a previously unscattered U nucleon. In this figure all yields are plotted in a log scale (in contrast to the square-root scale used in preceding figures). On the circle-point curves, statistical-uncertainty bars are shown wherever they would extend beyond the circle point. On the other curves, only a few samples of statistical-uncertainty bars are included. For further explanation see the text of Secs. IV. A and IV. C.

$d^2n/dE_N^{ES}d\Omega_N^{ES}$ plotted vs E_N^{ES}. The sensitivity to σ_{NN} is shown for three different angular groups. Of these three, the group involving largest yields is in the back-angle region ($\cos\theta_N^{ES} = -0.9$ to -1.0), where Figs. 14 and 15 show their thermal peaks. The medium-yield group (marked 123°) corresponds to $\cos\theta_N^{ES} = -0.5$ to -0.6, which is the general angular region where Figs. 14 and 15 indicate a transition between more-thermal and less-thermal character. The lowest-yield group (marked 0°–78°) stretches from $\cos\theta_N^{ES} = 1$ to $\cos\theta_N^{ES} = 0.2$ and thus corresponds to the near-isotropic portions of both the 70- and 130-MeV E_N^{ES} groups in Figs. 14 and 15. All the arrows in Fig. 16 mark the unique first-scattering energy $E_N^{ES} = 62.5$ MeV. However, the broad peaks at this energy are not associated with first scattering. (If they were, then the angular distribution would be isotropic and would be confined to a single E_N^{ES} bin.) Because the yield magnitudes vary so greatly, we have plotted all yields in Fig. 16 using a log scale, not a square-root scale. In the uppermost angular group the yield varies directly with σ_{NN}, in the middle group the yield varies little with σ_{NN}, and in the lowest angular group the yield varies inversely with σ_{NN}. As noted several times previously, direct variation suggests more-thermalized contributions while inverse variation suggests less-thermalized contributions.

V. SUMMARY AND COMMENTS

We have reported on a detailed examination of results calculated with a simple model: a much idealized though fully three-dimensional cascade model for $^{20}Ne + ^{238}U$. We have looked at gross features and studied their sensitivities to a few variations of the model. Our hopes are the usual ones—that the trends and sensitivities are reliable even if the absolute answers are not. The gross features considered are particle densities $\rho(\vec{r}, t)$ during collision, and emitted-particle distributions $d^2n/dEd\Omega$ after collision. Our sensitivity studies have involved variations of the impact parameter b_{NeU}, of the nucleon-nucleon cross section σ_{NN}, and of excluded-volume restrictions associated with a classical hard core in the NN interaction. Our excluded-volume feature is related to the incompressibility K and to "stiffness" as discussed in connection with equation-of-state treatments.[58] Also, our use of *alternative NN scattering styles* is analogous to the use of *alternative scattering-equivalent NN potentials* in many-body classical equations-of-motion calculations.[31] In presenting our sensitivity results, we have indicated some ways to pay careful attention to the uncertainties associated with converting digital-statistical in-

formation to continuous properties such as $\rho(\vec{r}, t)$ and $d^2n/dEd\Omega$.

For impact parameters $b_{NeU} = 0$ and 5 fm in $^{20}Ne + ^{238}U$, we calculate that during the collision, maximum compressions ρ/ρ_0 of about 2 or 3 may be achieved over spatial domains of ≈ 1 fm^3 and time spans ≈ 3 fm$/v_{BEAM}^{LAB}$. Quantitative results depend on details of the assumed NN scattering style and σ_{NN}. The maximum achieved compression generally increases as excluded volume decreases and as σ_{NN} increases. When the diameter of the excluded volume is changed from 0 to 0.5 fm (and when a restriction to in-plane repulsive scattering is concurrently invoked), then the maximum achieved compression decreases—from ≈ 2.5 to ≈ 2.1 when $\sigma_{NN} = 25.4$ mb, and from ≈ 2.9 to ≈ 2.5 when $\sigma_{NN} = 53.1$ mb. This suggests that $\rho(\vec{r}, t)$ might be somewhat overestimated by conventional cascade calculations that lack any excluded-volume feature (besides lacking any restriction to in-plane NN scattering).

Our maximum compressions ρ/ρ_0 calculated with $\sigma_{NN} = 25.4$ mb are similar to those found in (not-quite-analogous) calculations[28] for $^{238}U + ^{238}U$.

The sensitivity of ρ/ρ_0 to our NN interaction is mainly concentrated in the high-density interior region of the collided system. There is not much sensitivity in the low-density regions that form the periphery of the collided-matter system. Similarly, at times long after initial $^{20}Ne + ^{238}U$ contact, the emitted scattered-particle yields $d^2n/dEd\Omega$ show rather weak sensitivity to changes in our NN scattering style (provided that σ_{NN} is kept constant). This general result—that our NN scattering style influences transient insternal densities $\rho(\vec{r}, t)$ quite significantly, but influences end-of-collision asymptotic distributions $d^2n/dEd\Omega$ rather weakly—is reminiscent of results obtained in a recent classical-equations-of-motion (CEOM) study by Bodmer, Panos, and MacKellar.[31] In this CEOM study, two alternative scattering-equivalent NN potentials were used. In classical calculations for the collision of one nucleon with another, these two scattering-equivalent potentials give (by design) essentially the same asymptotic results. In classical calculations for colliding *many*-body systems (20 + 20 and 40 + 40), these two scattering-equivalent NN potentials lead to different density patterns $\rho(\vec{r}, t)$ during the collision, but to quite similar energy-angle distributions of particles emitted near the end of collision.[31]

We do find that our SIMON-calculated functions $d^2n/dEd\Omega$ are quite sensitive to changes in σ_{NN} from 15.4 to 25.4 to 53.1 mb. The character of the changes in $d^2n/dEd\Omega$ indicates that there are changes in the distribution of the number of scatterings suffered by a nucleon before being emitted. Such changes in scattering-frequency distribution were discussed only qualitatively in Sec. IV; because there we were concentrating on energy-angle-binned information, and at present we do not have energy-angle-binned information on the distribution of scatterings per emitted nucleon. In Table III now, we show some relevant information that we do have: energy-angle-*integrated* results for the scattering-frequency distributions as a function of $\{b_{NeU}$, style, $\sigma_{NN}\}$. Table III supports, explains, or extends some of the remarks made in Sec. IV about yields for $b_{NeU} = 0$ and 5 fm. For example, Table III indicates that the emitted-particle yields are more sensitive to σ_{NN} than to the NN scattering style; that an increased σ_{NN} leads to increased overall yield and to enhanced multiple scattering; and that a decreased b_{NeU} produces effects similar to those produced by increasing σ_{NN}. Table III tends to support a supposition made in Appendix A about b_{NeU}-integrated emission: that if our energy-dependent σ_{NN} is too small an effective cross section, then we underestimate the importance of multiple scattering (and so underestimate the post-collision proximity to global thermal equilibrium).

The simple-SIMON study reported in this paper was started with the idea of complementing, and guiding, improvements of the SIMON code to make it less idealized and more realistic. Meanwhile other cascade codes, with more realistic details, have been developed and shown to be economically feasible and also successful in reproducing many experimentally observed data.[21-23] Nevertheless, it still seems to us that the SIMON method has intrinsic advantages. In particular, SIMON 's method allows incorporation of the excluded-volume feature, and it obviates the need for a separate depletion or rearrangement recipe[59]—a recipe whose adjustment to fit experiment may obscure the importance of other physical effects. Therefore improvements in SIMON 's realism may still be very worthwhile. In any event, the results of our simple-SIMON study should be useful for several reasons:

(1) The role of excluded-volume effects has not been studied much, in other cascade-model work.

(2) Particle-density results have not been reported in as much detail, from other cascade calculations.

(3) The contribution of first-scatterings[60] to emitted-particle energy-angle distributions has been considered here in a way not reported for other cascade studies.

(4) Our sensitivity results for energy-angle yields argue against reliance on thermal-equili-

TABLE III. Ensemble-averaged number $N(\nu)$ of nucleons that have scattered ν times during a $^{20}Ne + ^{238}U$ collision. Above the dashed horizontal line, the entries are arranged to illustrate the insensitivity of $N(\nu)$ to NN scattering style. Below the dashed horizontal line, the entries are arranged to illustrate that with reference to the standard combination $\{b_{NeU}=0, \sigma_{NN}=25.4\}$, the effect of increasing b_{NeU} from 0 to 5 fm is similar to the effect of decreasing σ_{NN} from 25.4 to 15.4 mb.

Impact parameter b_{NeU} (fm)	NN scattering style	σ_{NN} (mb)	Cutoff time[a]	Ensemble size	$N(\nu)$ $\nu=0$	$\nu=1$	$\nu=2$	$\nu\geq 3$
0	RC	15.4	t_{STOP}	200	141	49	30	38
	4πI	15.4	t_{STOP}	300	148	42	27	41
	BB	25.4	$t(\infty)$	200	47	72	50	91
	BB	25.4	t_{STOP}	300	77	65	41	75
	RC	25.4	t_{STOP}	300	82	58	43	75
	4πI	25.4	t_{STOP}	300	93	49	34	82
	RC	53.1	t_{STOP}	200	15	40	48	155
	4πI	53.1	t_{STOP}	199	28	35	33	163
5	BB	25.4	$t(\infty)$	50	58	76	48	77
	BB	25.4	t_{STOP}	300	129	50	31	48
	RC	25.4	t_{STOP}	300	140	42	30	46
	4πI	25.4	t_{STOP}	300	143	41	29	45
5	RC	25.4	t_{STOP}	300	140	42	30	46
0	RC	15.4	t_{STOP}	200	141	49	30	38
0	*RC*	*25.4*	t_{STOP}	*300*	*82*	*58*	*43*	*75*
0	RC	53.1	t_{STOP}	200	15	40	48	155
5	4πI	25.4	t_{STOP}	300	143	41	29	45
0	4πI	15.4	t_{STOP}	300	148	42	27	41
0	*4πI*	*25.4*	t_{STOP}	*300*	*93*	*49*	*34*	*82*
0	4πI	53.1	t_{STOP}	199	28	35	33	163

[a] An entry $t(\infty)$ implies no time cutoff. An entry t_{STOP} implies cutoff at a time such that the center of an unperturbed Ne projectile would be 3 U radii past the center of an unperturbed U target.

brium or extreme single-scattering models, and instead support the idea that complicated intranuclear cascade calculations (incorporating detailed NN cross sections) are needed in order to describe the incompletely thermalized end-of-collision system.

(5) Our results from the billiard-ball model (of which only samples have been reported here) are available to be compared with results that could be calculated from a fluid-dynamic model for a hard-sphere gas. Such a comparison could teach us something about the effects of the instantaneous-local-equilibrium assumption in fluid-dynamic models.

Also, the goodness of "scaling" for experimental data has not been pointed out previously, to our knowledge. (See Figs. 2 and 3.)

What has been omitted from this study, but might be worth doing in the future? Several categories follow:

(a) straightforward extension of the present sensitivity studies (e.g., variation of σ_{NN} for collisions with $b_{NeU}=5$ fm);

(b) improvement of our SIMON models toward realism (e.g., to incorporate precollision Fermi motion, binding, and better NN cross sections);

(c) extension of the investigation to further observables (e.g., to multiplicity distributions and to particle-particle correlations);

(d) extension of the investigation to further currently unmeasurable features (e.g., to distributions of the number of scatterings suffered by nucleons emitted in specified energy-angle bins).

Other physicists are presently working on (b)–(d), to improve our simple SIMON models toward realism and then to extend their use.[29] We believe that substantial improvements over the realism of our simple SIMON models should be made before SIMON is used much to study other kinds of ob-

servables or nonobservables. We believe this because the correctness of many results will depend on the *balance* (i.e., on the degree of mutual cancellation) of various qualitative trends—and if the quantitative description is too sloppy, then correct balances can be achieved only by accident. Some of the aforementioned extensions (c), (d) have already been made, or could be made, with other (non-SIMON) codes that have many realistic features.[21-23] However, the most thoroughly developed of these other codes[21-23] do not incorporate the feature of excluded volume, and it would be good to allow this feature (as SIMON does), because its effects seem to be significant for density results. Of course SIMON and other cascade models share some of the same defects. For example, when compared with CEOM methods, SIMON and also conventional cascade[34] schemes are generally inferior in their treatment of potential-energy effects. Indeed, there are many realistic features—e.g., binding, precollision internal kinetic energy, and strong interactions at low *NN* energies—which present conceptual (and economic) difficulties for any cascade scheme proceeding by discrete *NN* scatterings. Cascade and CEOM methods have some important advantages over fluid-dynamic methods. Cascade and CEOM methods both avoid major assumptions about local and global equilibrium. Cascade methods, and to a lesser extent CEOM methods, allow the incorporation of information about experimentally determined *NN* cross sections. On the debit side, both of these mainly classical microscopic approaches, cascade and CEOM, may turn out to be less flexible than fluid-dynamic approaches for modeling some of the behavior associated with quantum mechanical aspects of a many-body system.[61] Also, cascade and CEOM methods may be less convenient than fluid-dynamic approaches for considering exotic phenomena, because exotic phenomena are often thought of in terms of the bulk properties of nuclear matter.

The preceding paragraph lists only some of the reasons why a variety of theoretical approaches, each having its own advantages and disadvantages, should still be used. Methods combining different approaches, e.g., combining microscopic and fluid-dynamic treatments, deserve special consideration and development.

ACKNOWLEDGMENTS

The author is grateful to V. E. Oberacker and T. A. Welton for many hours of helpful discussion. Thanks are due also to M. Gyulassy and C. C. Noack for advice on the manuscript. The research was sponsored by the Division of Basic Energy Sciences, U. S. Department of Energy, under Contract No. W-7405-eng-26 with the Union Carbide Corporation.

APPENDIX A: FURTHER DISCUSSION OF FIGS. 2 AND 3

We start by describing the energy-angle bins that were used in computing the SIMON BB distributions of Figs. 2 and 3. Then we explain how these bins broaden the SIMON first-scattering peaks. Finally, we discuss reasons for the deviations between theoretical and experimental results in Figs. 2 and 3.

The SIMON BB results in Figs. 2 and 3 could have been drawn as histograms, for these results were calculated using contiguous (E_{out}, θ_{out}) bins. Each bin had energy width 20 MeV $\equiv 20\times\frac{241}{250}$ ENU; and each had angular width 10° (for bins centered at 20°, 30°, . . . , 160°) or 15° (for bins centered at 7.5° and 172.5°). But instead of drawing histograms, we have assigned the average cross section within each bin to the median E_{out} and median θ_{out} of that bin, and then connected the resulting points with straight dotted lines.

SIMON's first-scattering one-to-one correspondence $\{E_{out}^{LAB}, \theta_{out}^{LAB}\}$ is given by Eq. (1). In Figs. 2 and 3, E_{out}^{LAB} and θ_{out}^{LAB} refer to an emitted nucleon-charge (in SIMON, an unbound proton). With the energy-angle bins described just above, the SIMON contributions that are assigned to $\theta_{out}^{LAB} = 30°$ consist of all scattered protons having θ_{out}^{LAB} in the angular span 25° to 35°. Then from Eq. (1), the corresponding first-scattering energies $E_{out}^{LAB}(\theta_{out}^{LAB})$ range over *three* neighboring energy spans. This explains the width of the BB peak at the 30° arrow in Fig. 2. Similarly, the first-scattering contributions that are assigned to 70° in Fig. 2 range over three neighboring energy spans; these stretch from 0 to 60 MeV (≡58 ENU) altogether. But in Fig. 3, all the first-scattering contributions assigned to a given median energy fall within a *single* energy-angle bin (one energy span, and also one angular span).

In Fig. 2 the smallest-energy portions of all the curves for $\theta_{out}^{LAB} = 70°$, 110°, and 150° have been omitted, both to avoid overlapping curves and because the SIMON model has several special problems there. Despite these problems in the small-energy region, the agreement with experiment is not so bad there. The 30° results at low energy are all included, and are typical of the magnitudes and agreements found at the other angles. The rest of this Appendix is speculative.

What about the serious disagreements between theory and experiment seen in Figs. 2 and 3 at back angles toward high energies? We propose

two principal causes. The first is our neglect of any internal kinetic energy of random motion within the precollision projectile and target. We have already mentioned (in Sec. II B) that in a real heavy-ion collision, initial Fermi motion broadens the one-to-one first-scattering correspondence $\{E_{\rm out}^{\rm LAB}, \theta_{\rm out}^{\rm LAB}\}$ that holds in simple SIMON. Initial Fermi motion is one kind of internal kinetic energy of random motion. As such, initial Fermi motion would permit first-scattering combinations $\{E_{\rm out}^{\rm LAB}, \theta_{\rm out}^{\rm LAB}\}$ with $E_{\rm out}^{\rm LAB}$ exceeding $(E/A)_{\rm BEAM}^{\rm LAB}$ or with $\theta_{\rm out}^{\rm LAB}$ exceeding 90°, two phenomena strictly forbidden in simple-SIMON first scattering. More generally, we can expect that for nucleons emitted after multiple scattering too, simple SIMON will underestimate the importance of high energies and backward angles in the laboratory frame. This is consistent with the general nature of the systematic deviation between SIMON BB results and experimentally determined results in Figs. 2 and 3. Indeed, for the kind of energy-angle distributions shown in Figs. 2 and 3 (decreasing exponentially with energy, at back angles toward high energies), an underestimate of the importance of back angles and high energies suggests an underestimate of the degree to which global thermal equilibrium has been attained. Global thermal equilibrium means a randomization of nucleon velocities in the overall ^{20}Ne + ^{238}U c.m. frame. Initial Fermi motion gives a head start toward attaining such randomization, so neglecting Fermi motion tends to underestimate that attainment.

Our oversimplification of the NN cross section may similarly give too weak a push toward a globally equilibrated spectrum, and this is the second cause which we propose for the systematic deviation between experiment and theory in Figs. 2 and 3. Suppose that our choice of σ_{NN} were an underestimate of the effective NN cross section. Then multiple scattering would not be promoted strongly enough; therefore global equilibrium would not be promoted strongly enough, and consequently we would underestimate the emitted-particle yield at back angles toward high energies. Without substantiating the entire argument, we explain here why we believe that our choice of σ_{NN} for Figs. 2 and 3 was an underestimate for some purposes.

The value $\sigma_{NN} = 25.4$ mb, which we used in the SIMON computations for Figs. 2 and 3, was chosen to be appropriate for *first scatterings*, at relative energies E_{NN} of several hundred MeV. But after nucleons have scattered a few times, their relative energies tend to be lowered, and for $E_{NN} \lesssim 100$ MeV the pertinent empirical cross sections are considerably larger than $\sigma_{NN} = 25.4$ mb. For example, for $E_{NN} \approx 50$ MeV a better choice would be $\sigma_{NN} \gtrsim 100$ mb.[35,30,31] Although this seems like a large difference, there exists a crude defensive argument for retaining the smaller σ_{NN} that is appropriate to first scatterings. That is, once a set of nucleons has become approximately thermalized, there is no great harm in underestimating the frequency of their scatterings with each other, because such scatterings will mainly exchange energy and momentum without seriously changing the overall velocity distribution. Still, it seems reasonable to suspect that $\sigma_{NN} = 25.4$ mb will incorrectly inhibit the approach to thermal equilibrium. [For small E_{NN}, there is some complication in choosing an optimum effective cross section $\sigma_{NN}(E_{NN})$. The choice is complicated by several considerations, e.g., by Pauli-principle effects and by the more doubtful validity of binary-scattering cascade models as σ_{NN} increases.]

Some other causes too may contribute to the systematic deviation of theory from experiment in Figs. 2 and 3. For example, a too-low σ_{NN} would suppress "shadowing." Shadowing promotes a tendency for escaped particles to be those whose last scattering set them *away* from the bulk of nuclear matter. Thus for a small projectile hitting a large target, shadowing tends to favor emission with $\theta_{\rm out}^{\rm LAB} > 90°$ at the expense of $\theta_{\rm out}^{\rm LAB} < 90°$. In this way, a too-low σ_{NN} would lead to an underestimate of the relative importance of larger $\theta_{\rm out}^{\rm LAB}$. Recall also that simple SIMON 's angle-independent σ_{NN} ignores the enhanced back scattering of Fig. 1. Of course, the detailed deviations between a realistic NN cross section and SIMON 's simple σ_{NN} may lead to a variety of quantitative deviations between SIMON 's results and experimentally determined heavy-ion reaction results.

In the preceding paragraphs giving possible reasons for experimental-theoretical deviations, we have emphasized emission at large $\theta_{\rm out}^{\rm LAB}$ and high $E_{\rm out}^{\rm LAB}$ because it is in these (smaller-yield) areas where Figs. 2 and 3 show the most pronounced deviations. Now we turn the discussion to low energies, $E_{\rm out}^{\rm LAB} \lesssim 50$ MeV. For small emitted energies, SIMON 's neglect of binding forces tends to allow the escape of nucleons that should really be bound in the residual target. The neglect of initial kinetic energy tends to compensate for this mistake. The neglect of enhanced forward NN scattering (Fig. 1) and of Coulomb scattering probably affects the emitted-proton yield most strongly at small angles and low energies.[62]

The scaling device used in Figs. 2 and 3 leads to fairly close agreement between the experimentally determined results at two different bombarding energies, $(E/A)_{\rm BEAM}^{\rm LAB} = 241$ and 393 MeV. The most remarkable agreement of this sort occurs for $\theta_{\rm out}^{\rm LAB} = 150°$, in Fig. 2. But this is just the region

of Fig. 2 where SIMON (which *suggested* the scaling device) gives its worst agreement with experiment. Recall that we have speculated above that SIMON fails at back angles partly because we neglect precollision Fermi motion. Note also that precollision Fermi motion is a fact (in addition to energy-dependent *NN* interactions, and relativistic mechanics) which spoils the exactness of the scaling device as an equalizer, for real heavy-ion collisions. Can the effects of precollision Fermi motion be important enough to disallow qualitative agreement between our SIMON results and the experimental results at 150°, and yet be so similar for $(E/A)^{\mathrm{LAB}}_{\mathrm{BEAM}} = 251$ and 393 MeV as to allow agreement between these two sets of scaled experimental data at 150°? At present, we do not know the answer.

Another unsettled matter is this: Which of the two bombarding energies, $(E/A)^{\mathrm{LAB}}_{\mathrm{BEAM}} = 241$ or 393 MeV, is more favorable *a priori* for agreement between SIMON's results and experimentally determined data? There are qualitative arguments on both sides. There should be better agreement with the 393-MeV data (i.e., worse agreement at 241 MeV) because SIMON neglects nuclear binding, precollision Fermi motion, Coulomb effects, and the Pauli and uncertainty principles. There should be better agreement with the 241-MeV data (i.e., worse agreement at 393 MeV) because SIMON neglects relativistic effects and pion production. Figures 2 and 3 show that in fact, the quality of fit turns out to be about the same at both beam energies.

Finally, let us make very explicit our diffidence about all the foregoing speculations. SIMON's oversimplifications may introduce enough errors *in varying directions* so that no great confidence can be placed in arguments, applied to specific energy-angle regions, which attempt to correlate the goodness of SIMON's assumptions with the goodness of SIMON's fits to experimental data.

APPENDIX B: FLUCTUATIONS AND CORRELATIONS DURING HEAVY-ION COLLISIONS

Here is a list of classical theoretical methods arranged, roughly, in order of increasing attention paid to fluctuations and nucleon-nucleon correlations during the course of simulating a heavy-ion-collision history:

One-fluid dynamics,
Boltzmann equation,
"Conventional" cascade schemes,
SIMON,
Classical equations of motion.

In the rest of this appendix we explain why we ordered the above list as shown.

Conventional one-fluid-dynamics methods deal with position-dependent particle densities $\rho(\vec{r}, t)$, momentum densities, and energy densities. However, these methods have nothing to say about particle-particle correlations within a single nucleus-nucleus collision, and they have very little to say about the position-dependent particle-momentum distribution.[63] One has to go outside fluid dynamics in order to interpret the energy density as implying either a second moment of particle momentum, or a full-blown local particle-momentum distribution (e.g., of Maxwell-Boltzmann form).[64]

The Boltzmann equation deals with a rather general single-particle distribution function $f_1(\vec{r}, \vec{v}, t)$. This implies greater flexibility than there is in fluid-dynamic approaches (even when the latter are extended by interpreting the energy density to imply a local momentum distribution, as suggested above). In particular, the Boltzmann equation involves particle-velocity moments going beyond the simple triad consisting of single-particle density $\rho(\vec{r}, t)$, mean velocity $\int \vec{v} f_1 d^3\vec{v}$, and width characteristic $\int v^2 f_1 d^3\vec{v}$. However, the Boltzmann equation by itself says nothing at all about particle-particle correlations. Many-particle correlation functions [e.g., two-particle correlation functions $f_2(\vec{r}_a, \vec{v}_a, \vec{r}_b, \vec{v}_b, t)$] do not appear in the Boltzmann equation.

Conventional cascade calculations use space cells, time steps, *NN* cross sections, and Monte Carlo methods. They describe the target matter that has not yet interacted with projectile matter, and/or the projectile matter that has not yet interacted with target matter, in terms of a not-yet-interacted density function ρ^{nyi} that is constant within each space cell (like a histogram). Discrete baryons are introduced, one or two per *NN* scattering, as the cascade process produces cascade particles resulting from interactions with the note-yet-interacted matter. The occurrence of such interactions depends on Monte Carlo procedures. These Monte Carlo procedures allow the production of ν discrete cascade baryons even in a space cell that, just before the production, had ρ^{nyi} times volume *less* than ν. This circumstance necessitates the use of a "depletion" or "rearrangement" prescription—a prescription which spreads the reduction of the density functions ρ^{nyi} over several or more cells so as to conserve the total number of baryons. Even when discrete cascade particles are involved, particle positions and event locations are described only by specifying the pertinent space cell. For example, the calculations do not involve detailed trajectories *within* a space cell. Conventional cascade calculations are often described as being based on the

Boltzmann equation, or being a way of performing Boltzmann-equation calculations. However, conventional cascade calculations do not suppress particle-particle correlations to the same extent that these correlations are suppressed in the Boltzmann equation. As indicated in our preceding paragraph on the Boltzmann equation, starting with a definite one-particle distribution function $f_1(\vec{r}, \vec{v}, t=0)$, a Boltzmann-equation calculation can lead only to a unique time-developed form $f_1(\vec{r}, \vec{v}, t)$. In contrast, a cascade scheme can be used to generate an ensemble of many different nucleus-nucleus collision histories. Therefore a cascade scheme does allow the evaluation of n-body distribution functions $f_n(\vec{r}_a, \vec{v}_a, \vec{r}_b, \vec{v}_b, \ldots, t)$ pertinent to one nucleus-nucleus collision. Because the initial conditions are not homogeneous in space, the functions f_n will in general differ from products of functions f_1. To put it another way, each cascade-calculated collision history involves a sequence of casually related abrupt-scattering NN events. Within each history, classical correlations are only *partly* suppressed, by the above-described uses of space cells and depletion-spreading volumes.[65]

SIMON, unlike conventional cascade calculations, simulates a heavy-ion collision by computing the position of every nucleon as a continuously traveling point in continuous three-dimensional space. During a simulated collision, no space cells or pre-established time steps are used (except insofar as each computer word has a finite number of bits). For the simulation of a heavy-ion collision, continuous density distributions are invoked only as the basis for a precollision Monte Carlo procedure which fixes initial point positions for all nucleons. This precollision Monte Carlo procedure introduces fluctuations of a sort not included in conventional cascade calculations; but this difference is probably not important. What is more significant is that SIMON uses no *ad hoc* depletion prescription, because there is no need to *spread* any density depletion. SIMON, unlike conventional cascade calculations, does introduce some correlations connecting the impact parameter $\vec{b}_{NN}$ in a microscopic event, with the NN state resulting from that microscopic event. (Details depend on which NN scattering style is chosen.) However, we make only the following mild claim that the presently included $\vec{b}_{NN}$ correlations are realistic: that there can be some reality introduced by virtue of an excluded-volume effect, and by virtue of a restriction to in-plane scattering. There are other aspects of SIMON's $\vec{b}_{NN}$ dependence which are not satisfying. That is, our present NN scattering styles introduce some unsatisfying correlations between prescattering $\vec{b}_{NN}$ and post-scattering nucleon trajectories. (For example, it is improper to use a style that describes all NN events as repulsive scatterings, and so never allows the distance of closest approach to be smaller than b_{NN}.) Apart from correlations involving $\vec{b}_{NN}$, because of the oversimplified σ_{NN} used in the present study our SIMON calculations ignore much of the experimentally observed correlation between prescattering energy E_{NN} and post-scattering velocity angles Ω_{NN}. In contrast, such correlations are now included in conventional cascade calculations that incorporate realistic cross sections $d^2\sigma_{NN}/dE_{NN}d\Omega_{NN}$.

Classical equation-of-motion (CEOM) methods use NN potentials. These NN potentials imply various spatial, energetic, and directional aspects of the NN interaction—aspects different from those that can be introduced by SIMON via σ_{NN} and hard-core considerations. Thus, it may be that CEOM methods can introduce some kinds of realistic correlations beyond those possible from abrupt-scattering cascade calculations.

Obviously, the above five paragraphs fall far short of describing all differences among classical methods. For example, some conventional cascade calculations neglect interactions between cascade particles, while SIMON has no such limitation. As another example, simple SIMON currently ignores an initial-density feature which some other calculations do take into account: diffuse edges of the initial colliding nuclei.

---

[1]A. Sandoval, H. H. Gutbrod, W. G. Meyer, R. Stock, C. H. Luckner, A. M. Poskanzer, J. Gosset, J.-C. Jourdain, C. H. King, G. King, Nguyen Van Sen, G. D. Westfall, and K. L. Wolf, Phys. Rev. C 21, 1321 (1980). For a very short history of theoretical developments, see paragraphs 2 and 3 of this experimental paper. For much more extensive reviews of experimental and theoretical work, see Refs. 2–10 below.

[2]S. Nagamiya, in *Proceedings of the Symposium on Heavy-Ion Physics from 10 to 200* MeV/AMU, edited by J. Barrette and P. D. Bond, Upton, New York, 1979, p. 131 (also available as Lawrence Berkeley Laboratory Report No. LBL-9494, 1979).

[3]D. K. Scott, Lawrence Berkeley Laboratory Report No. LBL-8931, 1979. (This is a set of lectures presented at the International School of Nuclear Physics, "Ettore Majorana" Center for Scientific Culture, Erice, Sicily, 1979.)

[4]A. S. Goldhaber and H. H. Heckman, Annu. Rev. Nucl. Part. Sci. 28, 161 (1978).

[5]J. R. Nix, Prog. Part. Nucl. Phys. 2, 237 (1979).

[6]M. Gyulassy, Fizika (Zagreb) 9, Suppl. 4, 623 (1977); and Proceedings of the EPS Topical Conference on Large Amplitude Collective Motion, Keszthely, Hungary, 1979, p. 601 (unpublished).
[7]Proceedings of the Symposium on Relativistic Heavy Ion Research, GSI, Darmstadt, 1978, edited by R. Bock and R. Stock, Report No. GSI-P-5-78 (1978).
[8]Proceedings of the 4th High Energy Heavy Ion Summer Study, 1978, Lawrence Berkeley Laboratory Report No. LBL-7766, UC-34C, CONF-780766, edited by C. Webb, J. Kingston, and J. Mahoney.
[9]Proceedings of the Topical Conference on Heavy-Ion Collisions, Fall Creek Falls, 1977, ORNL Report No. CONF-770602, edited by E. C. Halbert, J. A. Maruhn, V. Maruhn-Rezwani, and J. B. McGrory (1977).
[10]This was the mood at the Third Summer Study on High-Energy Heavy-Ion Physics held at Lawrence Berkeley Laboratory, 1976 (unpublished proceedings).
[11]G. D. Westfall, J. Gosset, P. J. Johansen, A. M. Poskanzer, W. G. Meyer, H. H. Gutbrod, A. Sandoval, and R. Stock, Phys. Rev. Lett. 37, 1202 (1976). There have been many extensions and refinements of the simple fireball model. See for example S. Das Gupta, Phys. Rev. Lett. 41, 1450 (1978); G. Mantzouranis, Phys. Rev. C 18, 2227 (1978); P. J. Siemens and J. L. Kapusta, Phys. Rev. Lett. 43, 1486 (1979).
[12]W. D. Myers, Nucl. Phys. A296, 177 (1978); J. Gosset, J. I. Kapusta, and G. D. Westfall, Phys. Rev. C 18, 844 (1978).
[13]J. Hüfner and J. Knoll, Nucl. Phys. A290, 460 (1977); J. Knoll and J. Randrup, *ibid.* A324, 445 (1979).
[14]R. L. Hatch and S. E. Koonin, Phys. Lett. 81B, 1 (1979).
[15]A. A. Amsden, J. N. Ginocchio, F. H. Harlow, J. R. Nix, M. Danos, E. C. Halbert, and R. K. Smith, Phys. Rev. Lett. 38, 1055 (1977). This letter reports results from several different theoretical models, compared with experimental results from bombardment of ^{238}U with ^{20}Ne at a Ne-beam energy of 250 MeV per nucleon in the laboratory. After this Letter was published, corrections were reported for its numerical information on the experimental results and on the intranuclear cascade 2 results. See Refs. 1 and 21 for the corrected versions.
[16]A. A. Amsden, F. H. Harlow, and J. R. Nix, Phys. Rev. C 15, 2059 (1977).
[17]A. A. Amsden, A. S. Goldhaber, F. H. Harlow, and J. R. Nix, Phys. Rev. C 17, 2080 (1978).
[18]J. A. Maruhn, T. A. Welton, and C. Y. Wong, in Oak Ridge National Laboratory Report No. ORNL-5137, 1976 (Physics Division Annu. Prog. Rep. 1975), p. 134; J. A. Maruhn and T. A. Welton, in Report No. ORNL-5306, 1977 (Physics Division Annu. Progr. Rep. 1977), p. 142; J. A. Maruhn, in Ref. 9, p. 156.
[19]H. Stöcker, J. A. Maruhn, and W. Greiner, Z. Phys. A 293, 173 (1979).
[20]H. H. K. Tang and C.-Y. Wong, Phys. Rev. C 21, 1846 (1980).
[21]R. K. Smith and M. Danos, in Ref. 9, p. 363.
[22]Y. Yariv and Z. Fraenkel, Phys. Rev. C 20, 2227 (1979).
[23]Y. Yariv and Z. Fraenkel, contribution to the Symposium on Nuclear Physics in Heavy-Ion Collisions between 10 and 300 MeV/Nucleon, Copenhagen, 1979 (unpublished).
[24]K. K. Gudima and V. D. Toneev, Yad. Fiz. 27, 658 (1978) [Sov. J. Nucl. Phys. 27, 351 (1978)]; K. K. Gudima, H. Iwe, and V. D. Toneev, J. Phys. G 5, 229 (1970).
[25]A. I. Baz, in Materials of the XII Winter School of LIYaF, Leningrad, 1977, p. 32 (Oak Ridge National Laboratory translation ORNL-tr-4653 by S. D. Blalock).
[26]J. D. Stevenson, Phys. Rev. Lett. 41, 1702 (1978).
[27]J. P. Bondorf, P. J. Siemens, S. Garpman, and E. C. Halbert, Z. Phys. 279, 385 (1976).
[28]J. P. Bondorf, H. T. Feldmeier, S. Garpman, and E. C. Halbert, Phys. Lett. 65B, 217 (1976).
[29]W. Jaisli, H. Kuhlman, and C. C. Noack, in Ref. 7, p. 365. This contribution reports various extensions of the simple SIMON code—extensions involving relativistic kinematics, Fermi motion in the initial nuclei, nuclear binding, and realistic *NN* cross sections. However, these extensions were not used in calculating the results reported by us in the present paper. (Yet further extensions of SIMON, and further applications, are being made by C. C. Noack and Y. Karant.)
[30]A. R. Bodmer and C. N. Panos, Phys. Rev. C 15, 1342 (1977); A. R. Bodmer, in Ref. 9, p. 309.
[31]A. R. Bodmer, C. N. Panos, and A. D. MacKellar, Phys. Rev. C 22, 1025 (1980).
[32]D. J. E. Callaway, L. Wilets, and Y. Yariv, Nucl. Phys. A327, 250 (1979); R. Babinet and L. Wilets, University of Washington report (1978).
[33]Without further qualifications, the terms "cascade," "classical equations of motion," and "rows on rows" are not mutually exclusive. However, we assume the following qualifications, so as to define three separate categories: We use "classical equations of motion" to characterize methods which invoke Newton's (or Hamilton's) equations of motion and which are capable of describing nucleons traveling under the influence of smooth *NN* potentials. We use "cascade" to charactize methods which describe nucleons traveling in straight-line paths that are interrupted by instantaneous scatterings sending the scattered products in new path directions.
[34]We distinguish between conventional cascade methods (e.g., Refs. 21–24) and other cascade methods (e.g., Refs. 25–29) as follows: In conventional cascade calculations for a heavy-ion collision, nucleons which have not yet been perturbed by the collision are described in terms of a finite probability density per unit phase space, rather than in terms of discrete nucleons. For further discussion see Appendix B.
[35]W. N. Hess, Rev. Mod. Phys. 30, 368 (1958).
[36]M. Sandel, J. P. Vary, and S. Garpman, Phys. Rev. C 20, 744 (1979).
[37]See also our Appendix A. Concerning the de Broglie wavelength, Ref. 27 may have been too gloomy on this subject. At $(E/A)^{\rm LAB}_{\rm BEAM}$=250 MeV, λ_{AB} is roughly equal to the internucleon spacing but $\lambda\!\!\!^{-}_{AB}$ is only $\approx\frac{1}{6}$ of the internucleon spacing (and the latter comparison is the more appropriate one).
[38]The results marked BB in Fig. 2 are from the same billiard-ball calculation as those marked "classical hard spheres" in Ref. 15. However, Ref. 15 displayed these billiard-ball results in comparison with older

experimental data (since revised).

[39]A. Sandoval *et al.*, Lawrence Berkeley Laboratory Report No. LBL-8771, 1979. The numerical data that were used for plotting the EST and OBS results in our Figs. 2 and 3 are the same as the data distributed with this LBL preprint (on a microfiche in a pocket pasted on the inside back cover). The published version of this preprint, *sans* microfiche, is Ref. 1. The numerical data can be ordered as an American Institute of Physics document; see the Report or Ref. 1.

[40]SIMON's emitted charges are all unbound protons. (See the first paragraph of Sec. IV.) The SIMON cross sections in Figs. 2 and 3 were calculated using a trapezoid rule and results computed at five discrete impact parameters b_{NeU}; see footnote (a) to Table II.

[41]Immediately after an abrupt "repulsive" scattering, the scattered particles are traveling *away* from each other. This definition of repulsive applies to scattering models (such as those in this paper) in which each two-body scattering involves a single, instantaneous change of the relative velocity of the participants but the positions of the participants are always well defined and continuous in time.

[42]See Ref. 41, but replace "repulsive" and "away" with "attractive" and "toward."

[43]Styles BB and 4πI are the same as the two extremes used in Refs. 27 and 28. Style RC is similar but not identical to RIHC of Ref. 28. Style RC conserves angular momentum in *some* individual NN scatterings (those in which $b_{\mathrm{NeU}} \leq 0.5$ fm), but RIHC never does (except by accident, with probability of measure zero).

[44]During a nucleus-nucleus collision SIMON calculates nucleon positions and nucleon velocities without using any space cells or pre-established time steps, except insofar as each computer word has a finite number of bits.

[45]This is the ρ_∞ of Ref. 27.

[46]See Ref. 27 for an alternative way ("functional fitting") to smooth the sum of delta functions.

[47]All contour plots were made with the help of the computer CØNPLT, described by B. A. Clark and R. H. Fowler, Oak Ridge National Laboratory Report No. ORNL/CSD-TM76 (to be published).

[48]Note that the noninfinitesimal volume elements are used only in computing ρ. See Ref. 44.

[49]There is a slight departure from perfectly uniform density because we impose a minimum on initial NN separations. See the next-to-last paragraph of Sec. II. C.

[50]A surface separations of 1.66 fm corresponds to a center separation of 12 fm.

[51]*Why is there a blank strip all along each z axis in Figs. 4–7?* These figures show contour plots of ρ during head-on collisions. For head-on collision $\rho_{\mathcal{S}}$ has cylindrical symmetry. Because of that, we compute ρ by averaging within cylindrically symmetric volume elements, and by assigning the average ρ in a given element to mesh coordinates which are the volume averages of $\tilde{r}$ and of z within that element. For Figs. 4–7 the volume elements of smallest $\tilde{r}$ are discs with outer radius $\Delta\tilde{r} = 0.8$ fm, and consequently volume-averaged radius $\tilde{r}_\mu = \frac{2}{3}\Delta\tilde{r} = 0.53$ fm. Since there are no mesh points with cylindrical radius <0.53 fm, the condition $\tilde{r} < 0.53$ fm defines a region where ρ/ρ_0 cannot be obtained by interpolating between values calculated at mesh points. Therefore we avoid drawing contour lines in this region of no interpolation; and the result is a blank strip along each z axis in Figs. 4–7. *Why is there no analogous blank area in Fig. 9?* For off-center collisions, the reflection symmetry of ρ dictates that we compute ρ by averaging within volume elements symmetric with respect to the xz plane, and by assigning the average ρ in a given element to mesh coordinates which are the volume averages of x, $|y|$, and z within that element. The associated region of no interpolation would be $|y| < 0.75$ fm; see the caption to Fig. 9. However, this region does not appear explicitly in the xz plotting area of Fig. 9.

[52]If we had not neglected internal kinetic energy of the precollision nuclei, then perturbation would propagate somewhat more rapidly within the collided system.

[53]Of course the microscopic behaviors underlying large $|\partial\rho/\partial z|$ are quite different for $\{4\pi\mathrm{I},\ 53.1\}$ and $\sigma_{NN} = 0$. For $\{4\pi\mathrm{I},\ 53.1\}$ the steepness is associated with a shocklike zone populated by scattered nucleons traveling in many different directions, with many different speeds. For $\sigma_{NN} = 0$ the steepness is associated with the sharp front of an overlap zone in which unperturbed Ne nucleons (all of velocity $\vec{v}_{\mathrm{NeU}}$) travel freely through unperturbed U nucleons (all at rest).

[54]The crossing segments are, typically, diagonals inside a small quadrilateral formed by contour lines. Within such small quadrilaterals our key patterns have been applied somewhat arbitrarily.

[55]In our coordinate system, 4.52 fm is the median x of the overlap region that would be swept out when a spherical ^{20}Ne projectile of sharp-edged radius $1.16\,A^{1/3} = 3.15$ fm traverses (without perturbation) a spherical ^{238}U target of sharp-edged radius $1.16\,A^{1/3} = 7.19$ fm, the impact parameter being $b_{\mathrm{NeU}} = x_{\mathrm{NeU}} = 5$ fm.

[56]Here is an illustration of how the fluctuations with angle change with E_p^{LAB}: In the left panel of Fig. 11, for $\theta_p^{\mathrm{LAB}} \leq 30°$, consider the circle points $\{\mathrm{RC}, 25.4\}$. Note the very strong similarity between their angular dependence at $E_p^{\mathrm{LAB}} = 70$ and 150 MeV. Such a similarity does not hold for any of the bins centered at 50, 90, 110, 130, or 170 MeV (as we conclude from results computed by us but not displayed in this paper).

[57]This qualitative result is so plausible that we have omitted any explicit evidence for it here in Sec. IV. However, quantitative evidence for it appears in Table III, within Sec. V.

[58]M. I. Sobel, P. J. Siemens, J. P. Bondorf, and H. A. Bethe, Nucl. Phys. A251, 502 (1975).

[59]See Appendix B.

[60]See Sec. II. B.

[61]C. Y. Wong and J. A. McDonald, Phys. Rev. C 16, 1196 (1977).

[62]There is at least one other feature of our computation which slightly suppresses emission at low energies. This is the t_{STOP} feature discussed in Secs. IV. A.1 and IV. A.3. However, Figs. 2 and 3 are rather little affected by this feature; see Sec. IV. A.3.

[63]A two-fluid model (see Ref. 17) introduces some rather restricted kinds of contributions to particle-particle (fluid-fluid) correlations, and to higher moments of the momentum distribution.

[64]In detailed fluid-dynamic calculations of heavy-ion collisions (see for example Ref. 16), the usual way to compute an emitted-particle energy-angle distribution

is to take into account the mean velocity but not the thermal energy of each fluid element. That is, it is assumed that every nucleon within a given fluid element has exactly the same velocity (equal to the fluid element's mean velocity) so that the post-collision emitted-particle energy-angle distribution has width only because different fluid elements have different mean velocities. This picture is very unlike the simplest fireball picture (Ref. 11), in which every matter element within the macroscopic fireball has the same mean velocity so that the post-collision emitted-particle energy-angle distribution has width only because there is a thermal distribution of aprticle velocities within each matter element.

[65]In Ref. 21 the depletion prescription is described as being self-consistent. In Ref. 22, two alternative depletion prescriptions were used: fast rearrangement (spreading the depletion over an entire nucleus) and slow rearrangement (small depletion-spreading volume).

[66]This is a comment to qualify paragraph 5 of Sec. II. A. Although exact backward scattering (like exact forward scattering) leaves the overall nucleon-momentum distribution unchanged, exact backward scattering (unlike exact forward scattering) does introduce some changes in fine details of the nucleon-momentum distribution as a function of nucleon position and nucleon charge.

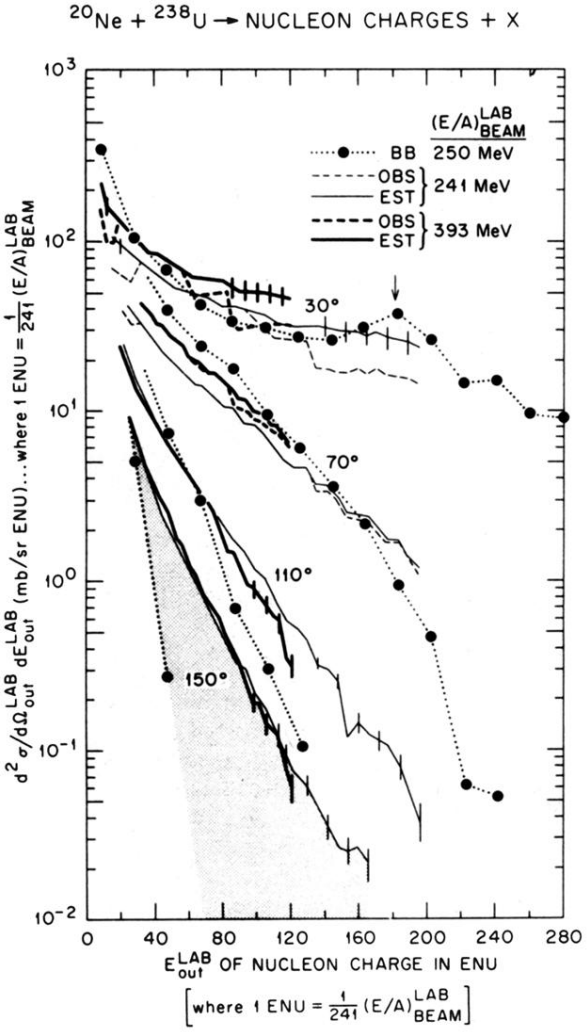

FIG. 2. Experimental and theoretical results plotted using energy units ENU, where 1 ENU = $\frac{1}{241}$ $(E/A)^{LAB}_{BEAM}$. Here SIMON 's billiard-ball model results (BB) are compared with the OBS (observed) and EST (estimated) results deduced by Sandoval *et al.* from their experimental data (Ref. 39). Where a solid line overlays a dashed line, the OBS and EST results essentially coincide. All the results are for inclusive double-differential cross sections describing emission of nucleon charges from the reaction $^{20}Ne + ^{238}U$. The energy units ENU are chosen proportional to $(E/A)^{LAB}_{BEAM}$, the laboratory beam energy per nucleon, because such a choice for energy units makes the BB results independent of $(E/A)^{LAB}_{BEAM}$. Some sample statistical-uncertainty bars are shown for the EST data, but only in those regions where the bar lengths exceed the diameter of the circle symbols marking BB points. In addition to the statistical uncertainties in the EST data, there is an uncertainty of ±20% in the absolute normalization. Where a displayed BB curve stops short of the right axis, its next point (and most succeeding points) would correspond to zero calculated yield (i.e., no counts in the bin).

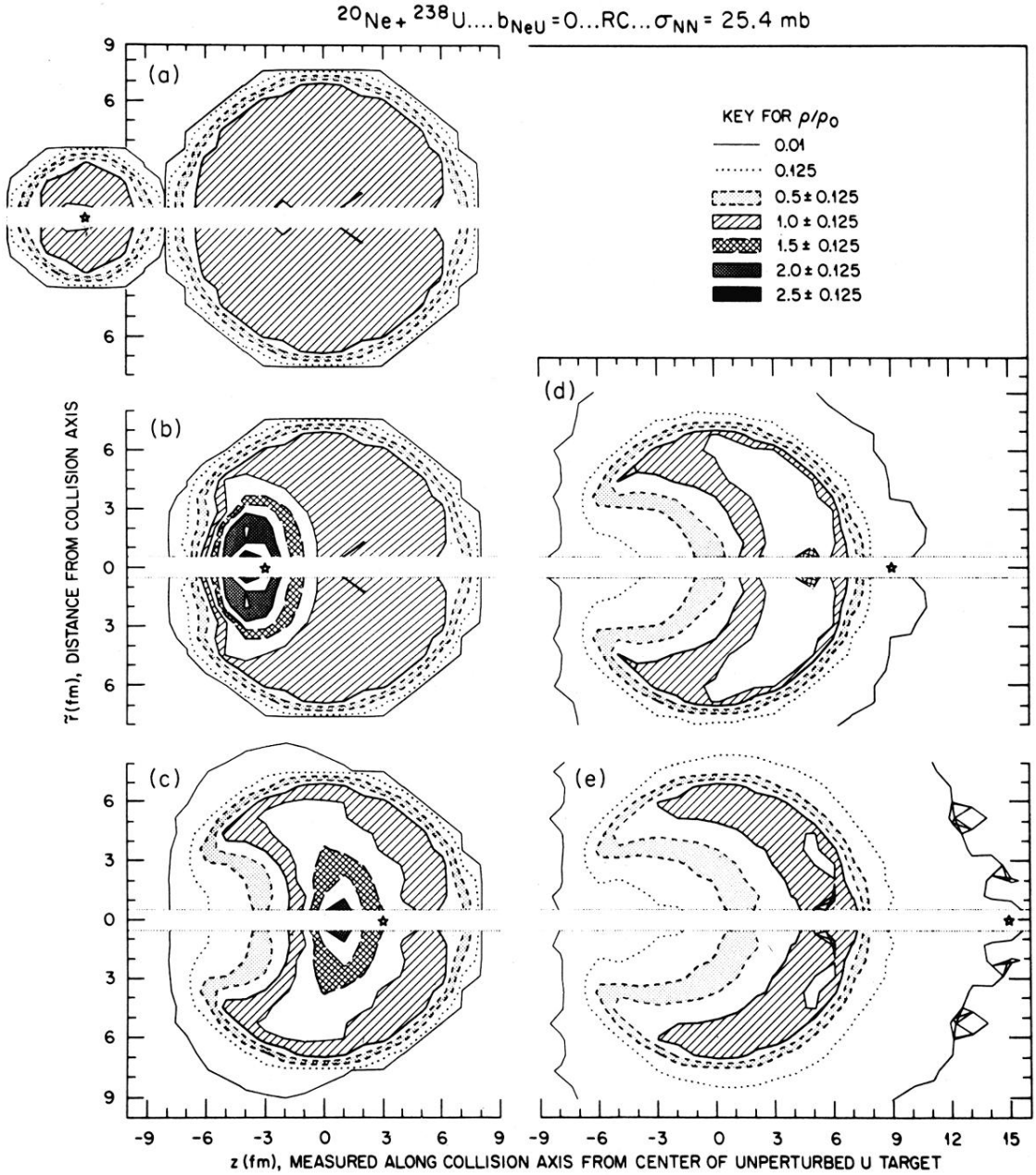

FIG. 4. Contour plots showing time development of the nucleon-matter density ratio ρ/ρ_0 during head-on collision of ^{20}Ne with ^{238}U. Each five-pointed star indicates time by showing where the center of an unperturbed Ne projectile would be. The densities ρ are obtained by averaging first within small finite volume elements, and then further over an ensemble of several hundred collisions (see Table I). Cylindrical coordinates $\tilde{r}$, z, and ϕ are used; and the space resolution is $\lesssim$1 fm because the volume elements are contiguous discs and rings each of dimension $\Delta\tilde{r} = 0.8$ fm, $\Delta z = 1.0$ fm, and $\Delta\phi = 2\pi$. The area keyed $(\rho/\rho_0) = 0.5 \pm 0.125$ is bounded by contour lines for 0.375 and 0.625, and similarly for the other keyed areas. Thus, in general, blank areas imply regions where ρ/ρ_0 could be estimated by interpolation. An exception is the no-interpolation blank strip along each z axis; there ρ/ρ_0 could be estimated by extrapolation but not by interpolation. For further explanation see the text of Secs. III. A and III. B.

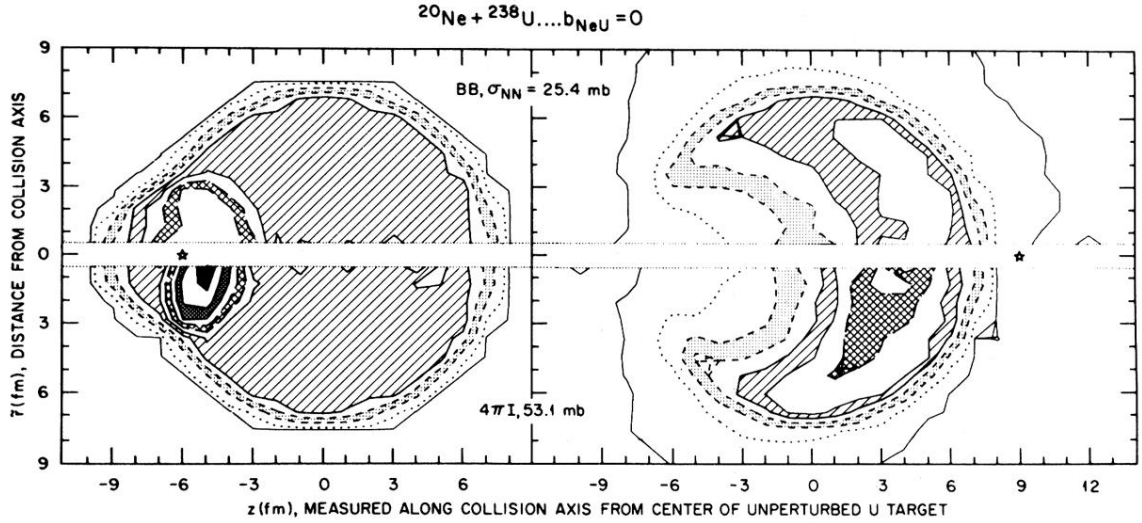

FIG. 5. Contour plots contrasting nucleon-matter densities calculated from two different NN scattering models: BB, 25.4 (upper) and 4πI, 53.1 (lower). The contrast is shown for both an early stage (left) and a late stage (right) during head-on collision of ^{20}Ne with ^{238}U. The key for ρ/ρ_0 is the same as that pictured in Fig. 4. For other conventions see the caption to Fig. 4 and the text of Secs. III. A and III. B.

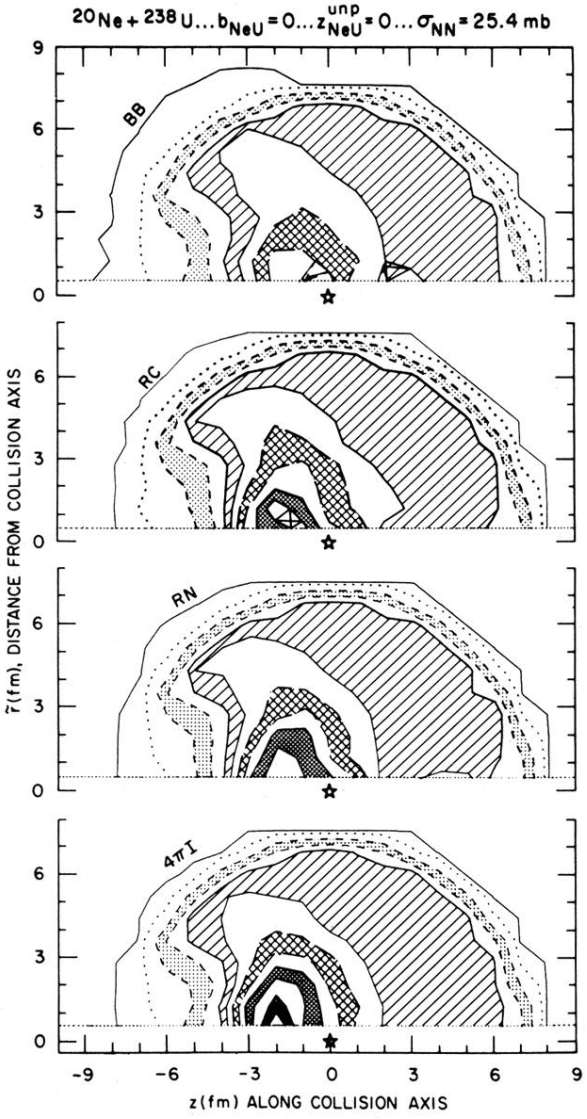

FIG. 6. Contour plots showing nucleon-matter densities calculated by using four different *NN* scattering styles (BB, RC, RN, and 4πI) all with the same *NN* cross section (25.4 mb). The comparison is made for head-on $^{20}Ne + ^{238}U$ collision at a time corresponding to $z^{unp}_{Neu} = 0$, i.e., when the projectile center would coincide with the target center if both nuclei were unperturbed. The key for ρ/ρ_0 is the same as that pictured in Fig. 4. For other conventions see the caption to Fig. 4 and the text of Secs. III. A and III. B.

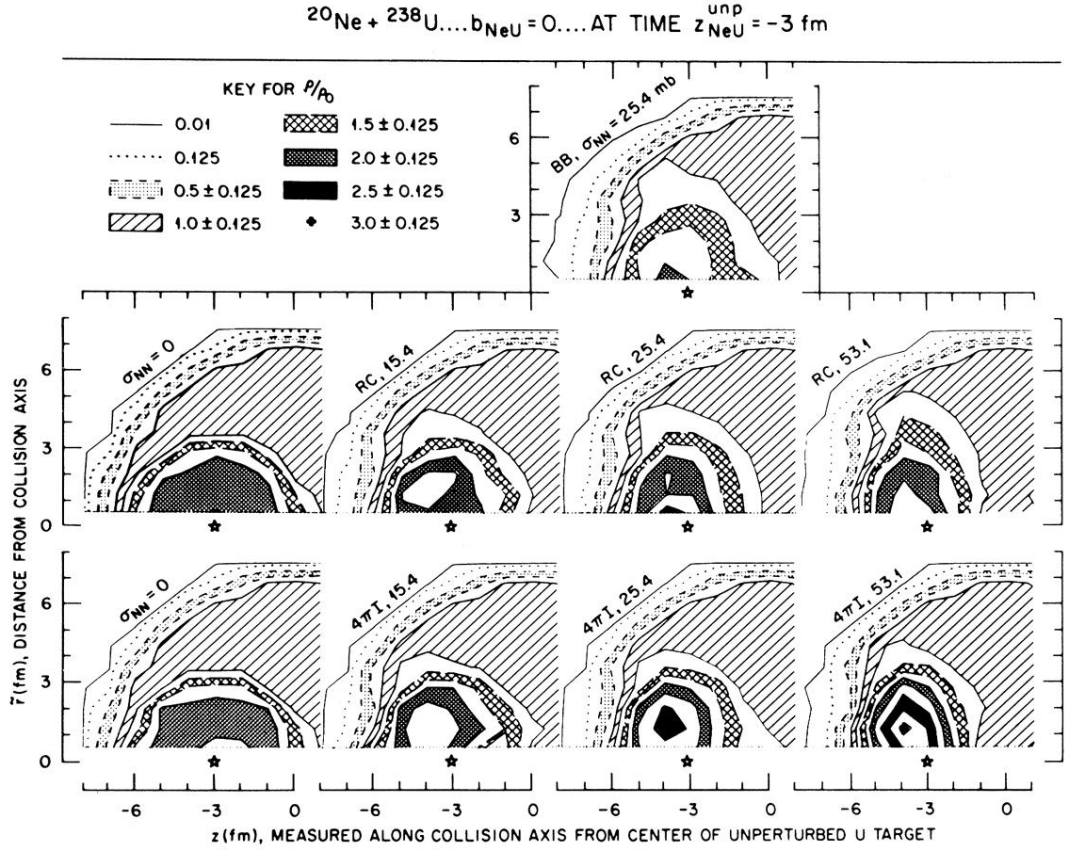

FIG. 7. Contour plots showing sensitivity of nucleon-matter densities to details of the *NN* model. Results are shown for three different *NN* scattering styles (BB, RC, and 4πI) used with various *NN* cross sections (σ_{NN} = 0, 15.4, 25.4, and 53.1 mb). All results are for head-on $^{20}Ne + ^{238}U$ collision at a time corresponding to $z^{unp}_{Neu} = -3$ fm, i.e., when the projectile center would be just 3 fm short of reaching the target center if both nuclei were unperturbed. (It is near this time that most of our models give their maximum ρ/ρ_0.) The bottom right diagram (4πI, 53.1) shows a small region (the innermost black-marked region) where $\rho/\rho_0 = 3.0 \pm 0.125$. For other conventions see the caption to Fig. 4 and the text of Secs. III. A and III. B.

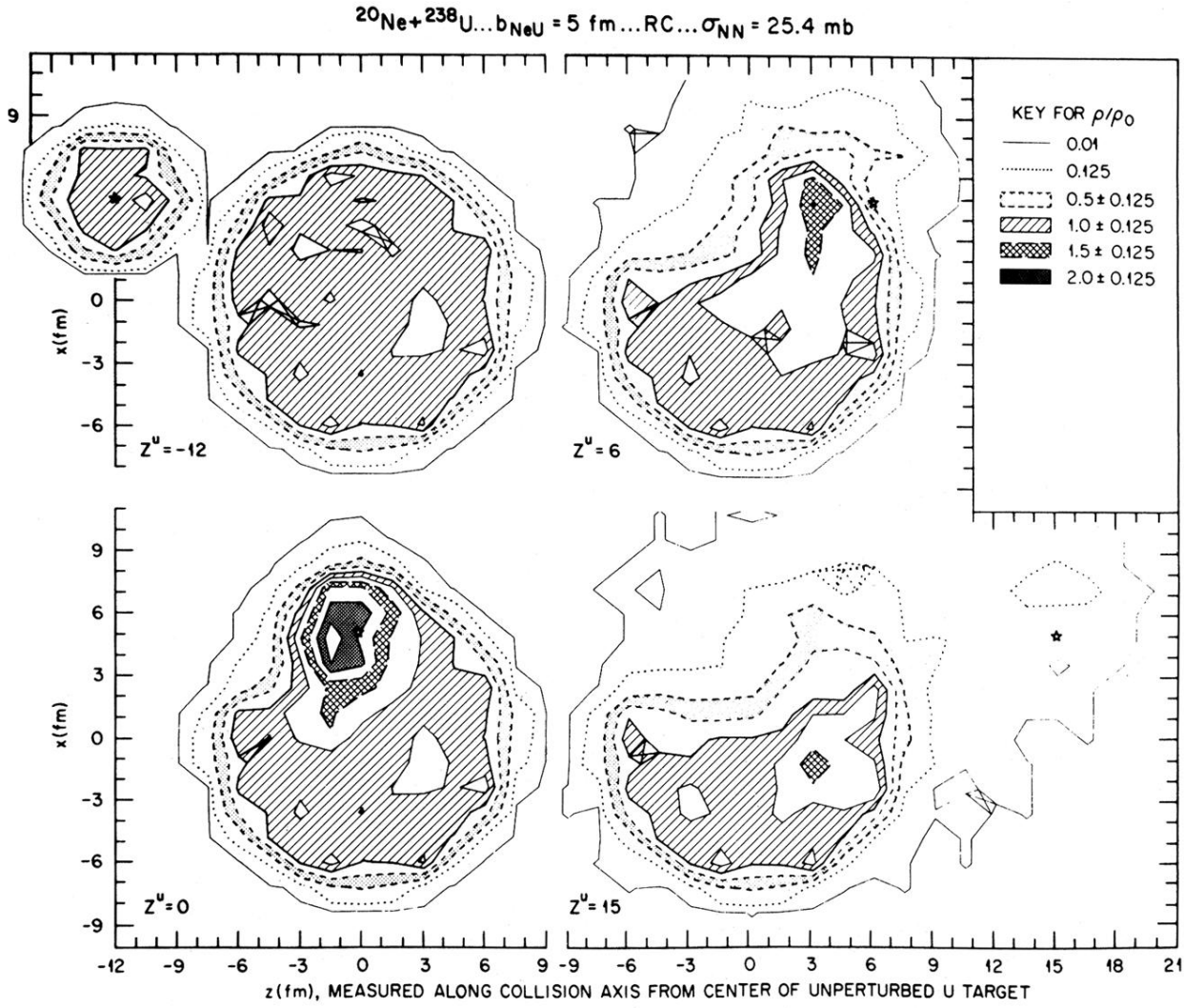

FIG. 9. Contour plots showing time development of the nucleon-matter density near the collision plane xz during $^{20}Ne + ^{238}U$ collision at impact parameter $b_{NeU} = 5$ fm. Each five-pointed star indicates time by showing where the center of an unperturbed Ne projectile would be. In contrast to the preceding figures, this figure uses Cartesian coordinates. The space resolution is $\gtrsim 1.2$ fm because the plotted densities are averages within contiguous volume elements each of dimension $\Delta x = 1.2$ fm, $\Delta y = 1.5$ fm, $\Delta z = 1.5$ fm, all lying within a slab of thickness $\Delta y = 1.5$ fm symmetric around the collision plane xz. Thus, each of these elements has a volume-weighted average $|y|$ of 0.38 fm (not 0). For further explanation see the text of Secs. III. A and III. B.